In situ radiographic and *ex situ* tomographic analysis of pore interactions during multilayer builds in laser powder bed fusion

Lorna Sinclair[1,2], Chu Lun Alex Leung[1,2], Sebastian Marussi[1,2], Samuel J. Clark[1,2], Yunhui Chen[1,2], Margie P. Olbinado[3], Alexander Rack[3], Jabbar Gardy[4], Gavin Baxter[5], Peter D. Lee[1,2]

[1] Department of Mechanical Engineering, University College London, WC1E 7JE, UK.
[2] Research Complex at Harwell, Rutherford Appleton Laboratory, Harwell, Didcot, OX11 0FA, UK.
[3] ESRF - The European Synchrotron, CS 40220, 38043 Grenoble Cedex 9, France.
[4] School of Chemical and Process Engineering, University of Leeds, LS2 9JT.
[5] Rolls-Royce plc, PO Box 31, Derby, Derbyshire, DE24 8BJ, UK.

Abstract

Porosity and high surface roughness can be detrimental to the mechanical performance of laser powder bed fusion (LPBF) additive manufactured components, potentially resulting in reduced component life. However, the link between powder layer thickness on pore formation and surface undulations in the LPBF parts remains unclear. In this paper, the influence of processing parameters on Ti-6Al-4V additive manufactured thin-wall components are investigated for multilayer builds, using a custom-built process replicator and *in situ* high-speed synchrotron X-ray imaging. In addition to the formation of initial keyhole pores, the results reveal three pore phenomena in multilayer builds resulting from keyhole melting: (i) healing of the previous layers pores via liquid filling during remelting; (ii) insufficient laser penetration depth to remelt and heal pores; and (iii) pores formed by keyholing which merge with existing pores, increasing the pore size. The results also show that the variation of powder layer thickness influences which pore formation mechanisms take place in multilayer builds. High-resolution X-ray computed tomography images reveal that clusters of pores form at the ends of tracks and when variations in the layer thickness and melt flow cause irregular

remelting and track height undulations. Extreme variations in height were found to lead to lack of fusion pores in the trough regions. It is hypothesised that the end of track pores were augmented by soluble gas which is partitioned into the melt pool and swept to track ends, supersaturating during end of track solidification and diffusing into pores increasing their size.

Keywords: Additive manufacturing, laser powder bed fusion, *in situ* X-ray imaging, Ti-6Al-4V, porosity

1. Introduction

Laser powder bed fusion (LPBF), also known as selective laser melting (SLM), is a rapidly evolving area of additive manufacturing (AM) technology using a layer by layer fabrication of 3D components from powder materials [1]. LPBF spreads layers of powder, which are then locally melted by a focussed laser beam according to a computer-generated programme. This process repeats until a full 3D part is produced [2]. The process is capable of producing components with complex geometries that cannot easily be made by conventional processing routes, *e.g.* casting [3]. The physics behind laser-powder interactions, *e.g.* the laser coupling to the metal surface and the melt pool dynamics, is very complex [4,5] and is related to both the material and process parameters.

Correlations between LPBF processing parameters and final part quality have been investigated through experimental [6,7] and modelling methods [8,9]. A number of studies have also investigated the transition from conduction melting to keyhole melting [10,11] as a function of process parameters. The volumetric energy density (*VED*) is defined by: $VED = P/vht$ [12], where *P* is the laser power, *v* is the laser scan speed, *t* is the powder layer thickness, and *h* is the hatch spacing. It is known that high energy density (*i.e.* high laser power coupled with low scanning speed) results in deep laser penetration (known as the keyhole mode) and often an increase in laser-induced features and spatter [13,14]. Very low energy density has been shown to produce wide, shallow melt pools, leading to discontinuous

tracks [15], interlayer porosity [16], and a heterogenous microstructure [17]. The microstructural evolution [18] and mechanical properties [19] of Ti-alloys produced by LPBF have also been investigated as a function of process parameters. However, most of the microstructural studies have been *ex situ* and do not reveal the underlying mechanisms controlling the development of the observed features.

A key area of interest in LPBF is the formation of internal porosity in the solidified structures. Lack of fusion [20], gas pores [21] and keyhole pores [10] are all known to occur in LPBF components. The former two pore types are also frequently found in electron beam melting AM [22,23]. Lack of fusion pores are often flat and elongated, arising from low energy density conditions where the prior track is not remelted. Gas pores are small and spherical and, for Ti-based alloys, may be due to the high solubility of hydrogen in the molten metal. Hydrogen gas can be absorbed from water vapour or contamination associated with the powder or the environmental chamber [24]. During cooling, the hydrogen solubility rapidly decreases and gas pores can nucleate in the melt [25,26]. The rapid cooling rates do not allow for diffusion and pore growth before solidification [27–29] and pores have been observed to be 10 – 300 μm in diameter. Pre-existing gas pores in the powder particles, arising from the atomisation manufacturing process, can also be a source of porosity in LPBF tracks. These pores can be entrained into the melt pool and can coalesce into larger pores [30,31].

The keyhole melting regime [32], although producing efficient energy transfer, can lead to the formation of keyhole pores [33] when a metal vapour/gas-filled bubble becomes trapped due to melt pool oscillations, unstable keyhole walls [34], or other complex hydrodynamic behaviour [35]. These bubbles can be composed of trapped inert chamber gas [4], metal vapour [10], or a combination of both. They are usually located near the bottom of the keyhole because rapid solidification prevents them from rising to the top of the melt [33,36].

A lack of understanding of the complex laser-matter interactions present during LPBF, including the formation of a dynamic melt pool, spatter (powder and droplet), metal vapour, plasma, and irregular powder entrainment [37], is hindering a more widespread uptake of LPBF technologies and thus further investigations are needed to help resolve this. Much of

84 the porosity analysis work has been carried out by *ex situ* studies, supported by computational
85 models, to investigate formation hypotheses. *In situ* experiments with synchrotron X-ray
86 radiography can provide critical information to substantiate these models and theories [38] by
87 observing process phenomena such as spatter [39], melt pool flow [37,40], melt pool size
88 [34,41], keyhole melting [36,42] and porosity formation [32,43–45] .

89 *In situ* laser melting experiments on a solid substrate have determined a relationship
90 between the laser power and scan velocity, and the transition from conduction to keyhole
91 mode melting regimes, causing a change in the shape of the melt pool and keyhole [34]. In
92 the case of LPBF, laser beam spot size and powder layer thickness can also affect the energy
93 density transition to keyhole melting [10]. Deep, narrow cavities were described as the
94 unstable keyhole zone, which led to the formation of keyhole pores [34]; the depth of these
95 pores increased as energy density increased [42]. High-speed X-ray imaging has been used
96 to observe the formation of these keyhole pores *in situ* during laser scanning [32,42,43,46].

97 Pore movement within the melt pool has also been observed during LPBF [37,47] by *in*
98 *situ* studies. Pores were shown to be swept with the Marangoni flow of the molten pool [37].
99 Pore shrinkage [42] and spheroidization [32] during solidification are other phenomena
100 observed via X-ray imaging. Furthermore, oxidised powder has also been shown to
101 significantly increase the internal porosity content [40], which is a key concern for reactive
102 metals such as titanium and aluminium. These *in situ* studies have also been supplemented
103 with porosity analysis via micro-computed tomography (μCT) [16,30,48–50].

104 However, to date, most *in situ* synchrotron studies of the melt pool and pore formation
105 in LPBF have involved the melting of a single layer of material. Experiments have been carried
106 out on: a range of materials in overhang (melting onto powder) conditions [37,40,51]; a bare
107 substrate without powder [34]; and on a substrate with a single layer of powder [32,36,41–44].
108 Since LPBF components are formed by many layers deposited on top of one another, an
109 understanding of the multilayer process is essential. In the present study, we characterise
110 multilayer builds *in situ* using high-speed synchrotron X-ray radiography, capturing the rapid
111 dynamics of laser remelting, layer cohesion (or lack thereof), and changes in pore formation.

To conduct this work, a laser AM *in situ* and *operando* process replicator (ISOPR) [37] was developed to build multilayer tracks *in situ* during LPBF. The building of multilayer thin walls on a substrate was observed using four processing conditions (which gave a range of energy density values), and the influence of the powder layer thickness has also been investigated. The keyhole operating mode was selected as there is a need for a better understanding of porosity formation, and whether it can be controlled or minimised in this mode. Additionally, the track morphology and internal porosity were characterised *ex situ* by μCT, to measure pore sizes and distributions, and better understand how changing the energy density can minimise pores and optimise track morphology.

2. Methods

2.1 Materials

Commercially pure (CP) titanium substrates with dimensions of 46 mm x 17 mm x 0.3 mm were used throughout this study. 0.3 mm substrate thickness was selected as the best compromise between realistic build conditions and sufficient X-ray transmission for good image quality. The melt pool width is less than the substrate thickness, so the influence of the walls is minimal, and the overall effects of sample dimensions on the powder bed is negligible [37].

Gas atomised (GA) Ti-6Al-4V powder (supplied by Goodfellow, UK) with a particle size distribution of 15 – 45 μm was selected. The powder morphology was examined by scanning electron microscopy (SEM) in secondary electron imaging mode at 20 kV (JEOL JSM-6610LV, Tokyo). **Figure 1a** shows an essentially spherical morphology of powder, with few satellite particles. The particle size distribution was measured using a Mastersizer 2000 laser diffractometer (Malvern Instruments Ltd., UK). **Figure 1b** displays the cumulative size distribution plot for the powder where the D_{10}, D_{50}, and D_{90} symbols represent the particle diameters for 10 %, 50 %, and 90 % of the cumulative volume (%). The size distribution and the median (D_{50}) particle size are representative of those typically used in LPBF.

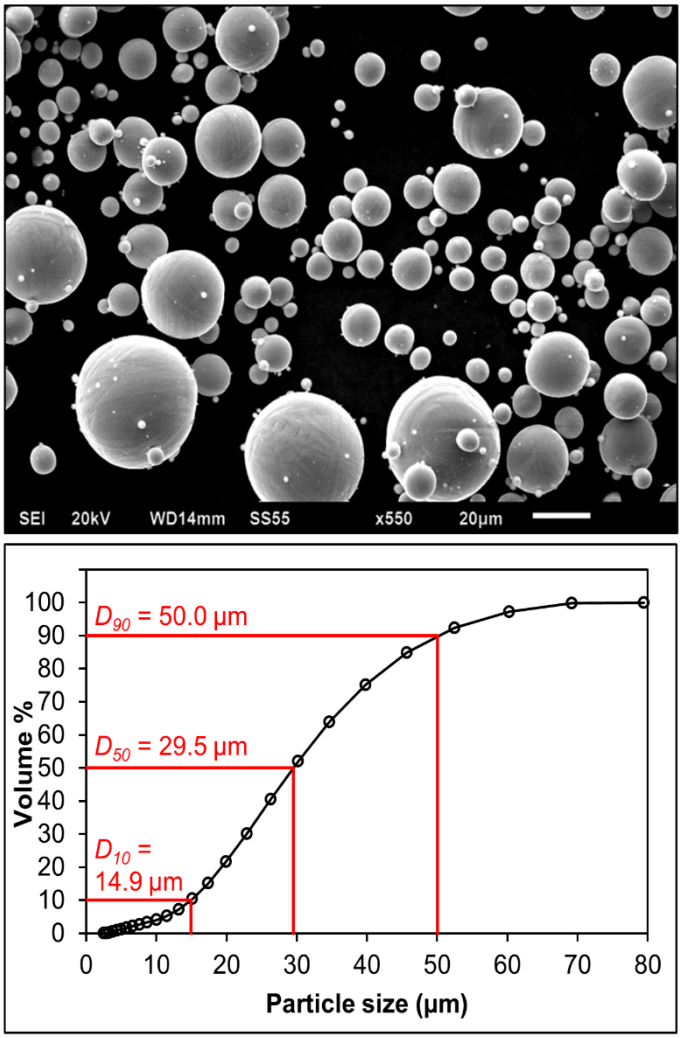

138

139 ***Figure 1**: (**a**) SEM image of Ti-6Al-4V gas atomised powder particles used in this study. (**b**)*

140 *Cumulative powder particle size distribution with D_{10}, D_{50}, and D_{90} labelled as determined by*

141 *laser diffractometry.*

142

143

2.2 *In situ* and *operando* process replicator

The experimental setup consists of a laser additive manufacturing *in situ* and *operando* process replicator (ISOPR) [37]; a small scale laser powder bed system, with the ability to produce multilayer parts. The ISOPR consists of: a continuous wave 200 W Yb-doped fibre laser, with a wavelength of 1030-1070 nm (SPI Lasers Ltd, UK); an environmental chamber (**Figure 2a**) containing a powder bed with 40 – 60 % powder packing density; and a series of laser beam optics, namely a collimator, beam expander, and an *X*-*Y* galvanometer scanner to control the laser line scanning, with an f-theta lens to focus the laser to a *ca.* 50 μm diameter spot ($4\sigma_{xy}$) [37]. The environmental chamber was evacuated and backfilled with argon gas at a constant flow rate of 4 l min^{-1} during experiments to maintain an inert atmosphere and prevent oxidation of the powder and molten pool.

The powder bed sample holder (**Figure 2b** and **c**) encases the substrate between two glassy carbon (GC) plates, which are used for their near transparency to X-rays. For each layer, the substrate is lowered by a pre-set layer thickness of 100 μm, and the cavity between the GC plates is filled with Ti-6Al-4V powder using a vibrating gravity-fed powder hopper. A scraper behind the powder hopper ensured an evenly levelled powder surface on the deposited layer. This process is repeated for each subsequent layer in a build for 5 layers.

2.3 Experimental build conditions

Four processing conditions were selected, detailed in **Table 1**, henceforth referred to as Sample A, B, C, and D. Typical LPBF powder layer thicknesses range from 20 – 100 μm [52], however recent studies have investigated powder layers up to 250 μm for improved build rate [53,54]. 100 μm was selected for this study for the best radiography image quality within the standard operating range. The nominal linear energy density (*LED*) was calculated for each condition: $LED = P/vt$ [17], where *P* is the laser power, *v* is the scan velocity, and *t* is the powder layer thickness. *LED* is an adaptation of the volume energy density (*VED*) equation [12] where a single track was employed, and thus hatch spacing (*h*) was equal to 1. **Supplementary Table 1** shows some examples of typical LPBF operating conditions and *LED*

values for comparison to the present study. The calculation shows that the energy density of this work is within the range used in typical industrial LPBF machines. *VED or LED* have been used in a number of studies [37,55–61] to correlate possible links between processing parameters, resultant energy densities, and build quality. However, *VED* and *LED* are not necessarily a reflection of absorbed energy density, due to powder ejection, and laser reflections within the keyhole [62] for example. The calculation also does not capture complex physics and is thus limited [55].

The ISOPR was employed to build a single line scan per layer for 5 layers onto a CP Ti substrate using a bi-directional scan strategy, alternating scan direction with each deposition layer. Layers 1, 2 and 5 were captured by synchrotron X-ray radiography. In the case of Sample A, a snapshot of the final track morphology was also recorded after layers 3 and 4.

2.4 *In situ* synchrotron X-ray radiography

In situ X-ray radiography experiments were carried out at the ID19 imaging beamline at the ESRF - The European Synchrotron, Grenoble, France [63]. The hard X-ray beamline uses a polychromatic beam, produced by two U32 undulators. The mean energy was *ca.* 30 keV. The attenuated X-ray beam was converted into visible light using a 200 µm thick LuAG:Ce scintillator (Ce-doped Lu_3Al_5O_12, Crytur, Czech Republic) and images were recorded with a FASTCAM SA-Z 2100K (Photron, USA) 4x magnification, at 40,000 fps, an exposure time of 12.6 µs and an effective pixel size of 4.76 µm. The field of view was 4.8 mm (width) x 2.4 mm (height).

2.5 Micro-computed Tomography (µCT)

All samples were examined post-build by µCT using a Nikon XTH225 (Nikon, Japan) to image and quantify internal porosity, **Figure 2d**; 3175 projections were collected, each with an exposure time of 1 s. The data was reconstructed using filtered-back projection and beam-hardening algorithms embedded in CT Pro (Nikon), resulting in a voxel size of 2.7^3 µm^3 [51]. The image analysis was performed using Avizo 9.3 (ThermoFisher Scientific). A kernel of 3 x 3 x 3 median filter was applied to remove noise, and a threshold applied to analyse internal

pores [50]. Any pore with a volume of < 27 voxels was discounted from the analysis. Pore volume was converted from the number of voxels to equivalent diameter (D_{eq}) using the equation:

$$D_{eq} = \sqrt[3]{\frac{6V}{\pi}}$$

where V is the volume of the pore [50] and hence 27 voxels is approximately a D_{eq} of 10 µm.

Pore sphericity, ψ, was calculated using the sphericity equation [64]:

$$\psi = \frac{\pi^{\frac{1}{3}}(6V_p)^{\frac{2}{3}}}{A_p}$$

where V_p is the volume of a pore, and A_p is the surface area of a pore. Sphericity of pores with very small volume could exceed a value of 1 because the surface area measurements in Avizo 9.3 are based on chordal approximations, whereas volume measurements use the number of voxels and no approximations; this effect is more prevalent as voxel number reduced [65].

2.6 Image analysis

The open-source software Fiji version 1.52i [66] was used to analyse radiographs. 100 flat-field and 100 dark-field X-ray images were collected. The acquired radiographs were normalised using the flat-field correction (FFC) equation: $FFC = \frac{I - Dark_{avg}}{Flat_{avg} - Dark_{avg}}$, where I is the raw image, $Dark_{avg}$ is the average of 100 dark-field images, and $Flat_{avg}$ is the average of 100 flat-field images [37]. This removed artefacts and noise variations inherited from the acquisition process. Local averaging over 50 neighbouring frames, 25 before and 25 after, was used to increase the contrast to reveal key features such as the laser keyhole, and remove stationary features; background subtraction using the first 50 static frames highlighted the deposited powder layer, shown in **Figure 2e.**

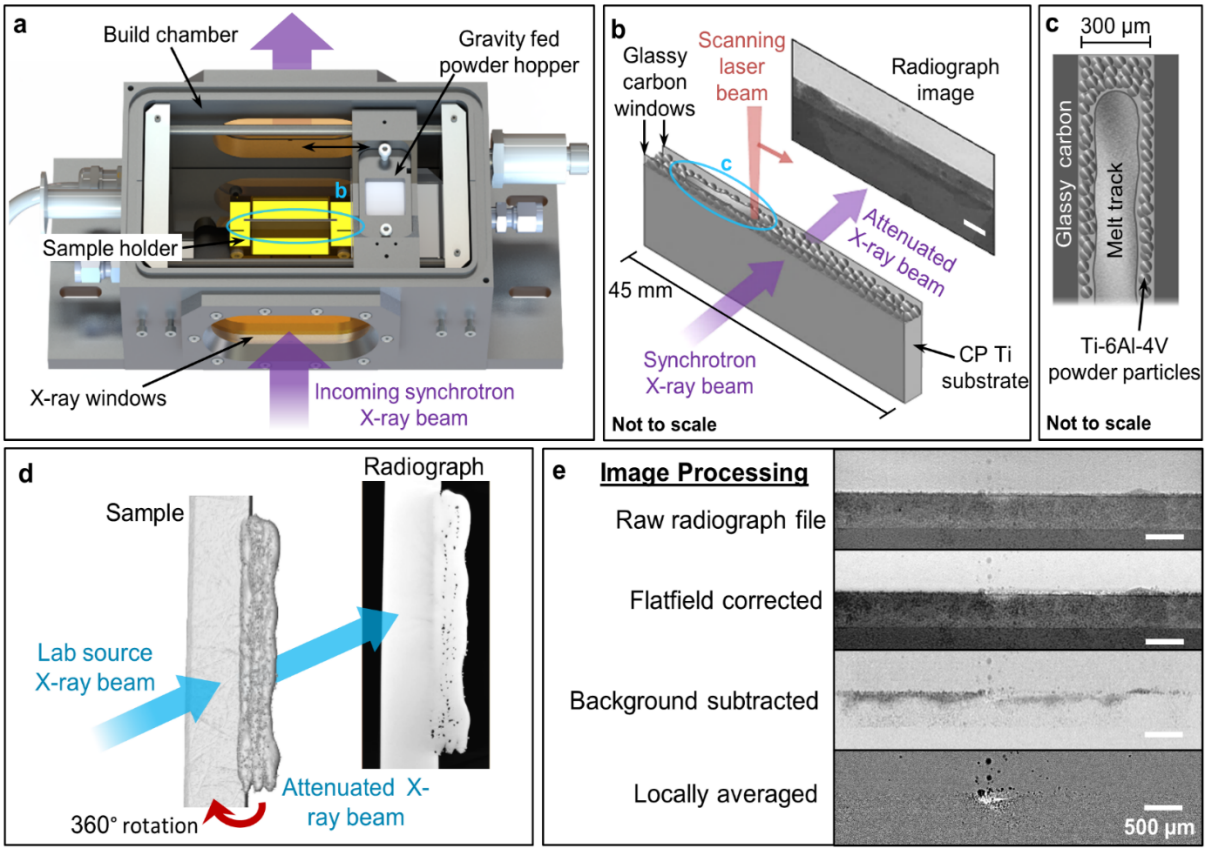

Figure 2: *(**a**) Experimental build chamber with key components labelled. (**b**) Simplified schematic of the sample holder during in situ melting. (**c**) Schematic of the substrate and powder particles and melt track. (**d**) Schematic of µCT sample scans. (**e**) Image processing methods.*

***Table 1**: Four target processing conditions selected to give different (LED) values.*

Sample ID	Laser power, *P* (W)	Scan velocity, *v* (mm s^{-1})	Nominal powder layer thickness, *t* (μm)	Nominal *LED* (J mm^{-2})	Average powder layer thickness, t_m, of the fifth layer (μm)	Adjusted *LED* (J mm^{-2})
A	150 ± 1	200 ± 1	100	7.5	119 ± 50	6.3
B	200 ± 1	200 ± 1	100	10	115 ± 45	8.7
C	200 ± 1	300 ± 2	100	6.7	139 ± 35	4.8
D	200 ± 1	400 ± 3	100	5	163 ± 50	3.1

3. Results

Table 1 lists the *LED* values for the target processing conditions. The nominal *LED* was calculated using the desired powder layer thickness of 100 μm. The average powder layer thickness measured, t_m, was obtained from the background subtracted radiograph images, with a threshold used to separate the powder layer. The powder thickness variation along the length of the track (shown later in **Figure 4f** and **Supplementary Figure 1**) was averaged, and standard deviation calculated. t_m was used instead of the nominal value *t* to calculate an adjusted *LED, as* t_m was larger than *t* for every condition. Previous studies have similarly observed thicker than intended powder deposition layers [67], however the disparity was due to the powder consolidation ratio rather than variations in track height as seen here. Typical *LEDs* used in previous literature are shown in **Supplementary Table 1.** The adjusted *LED* was thus lower than the nominal *LED* for every sample. This indicates that for multilayer builds, in addition to the aforementioned limitations of the *LED* calculation, the variation in powder thickness is another reason why *LED* is not necessarily a reliable method for quantifying absorbed laser energy density.

Initial observations of the radiographic data showed a large amount of powder spatter, as has commonly been seen in LPBF [39], caused by metal vapour jetting [68]. Powder entrainment into the jet can locally reduce the powder layer thickness ahead of the laser [69], and hence the laser beam can penetrate deeper into the previously deposited material. Due

to the nature of the sample holder, some excess powder was visible in the X-ray direction between the substrate and GC windows, along the entire length of the sample, and also on top of the GC windows. In some instances, this reduced the visibility of internal features such as pores. In multilayer builds, the track height was seen to vary along the length of the track, resulting in the large variation of powder layer thickness measured.

3.1 Multilayer track morphology

Figure 3 shows radiographs of a representative sample (Sample A) at various stages of the build. Background noise and excess powder has been removed in radiographs (b – d) to highlight the track shape. Unedited final track radiographs are in **Supplementary Figure 2** (layer 3), and **Supplementary Videos 1** and **2** (layers 1 and 5 respectively). Layer 1 shows a uniform build height, largely free from undulations. Layer 3 shows a distinct undulating surface morphology along the length of the sample. Layer 5 shows an uneven surface but a reduction in amplitude of the undulations compared to layer 3.

The surface undulations significantly changed the thickness of subsequent powder layers, as the largest peak-to-trough distance was *ca.* 220 μm (Layer 3). Furthermore, local denudation, caused by recoil pressure and powder entrainment into metal vapor plumes [36,69], was more extensive where the powder layer was thinnest, (*e.g.* at the undulation peak) as vapour plumes are likely to eject a larger fraction of the available powder.

An uneven track surface also changed the depth of remelting of the previous layer along the track length. Each new powder layer was spread out with a level surface over the previous build. As the laser penetration depth was *ca.* 150 μm below the powder surface for Sample A, the peaks of the surface undulations – with less powder covering them – underwent deeper remelting than the troughs. Lack of fusion may have occurred when the laser penetration depth was less than the powder layer thickness.

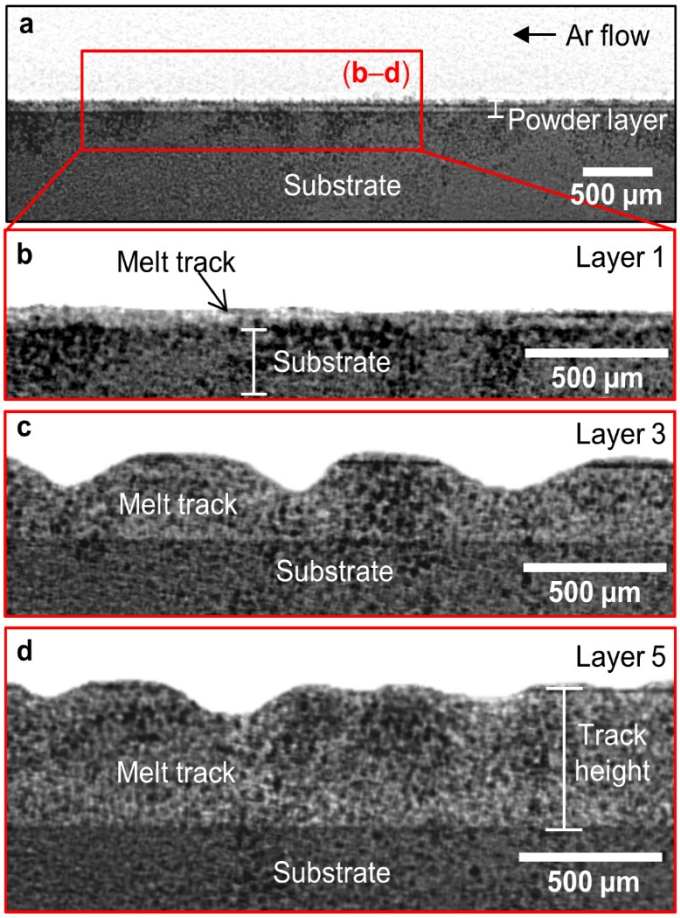

***Figure 3**: Radiographs of final multilayer track morphologies in Sample A. **(a)** Full substrate length with added powder layer (100 µm), and highlighted red region of interest for **(b)**, **(c)** and **(d)** which show final melt track morphology in layers 1,3 and 5 respectively, with prominent surface undulations.*

Figure 4 shows a time-series set of radiographs taken during the deposition of layer 5 in Sample B, with evidence of undulations in track height and powder layer. **Figure 4a** shows the large variation in powder layer thickness spread on top of the previous 4 solidified layers (yellow dotted outline). **Figure 4b** shows evidence of keyholing during the process; *ca.* 1.2 mm along the substrate, where the powder layer is around its thickest (*ca.* 200 μm, **Figure 4f**). The purple dashed line in **Figure 4c** outlines the layer 5 track surface. The thickness added by the deposition of layer 5 is revealed by the difference between the dashed (purple) and dotted (red) lines. The keyhole extends *ca*. 350 μm below the track surface (**Figure 4d** and **e**). It is clear from these images that laser penetration extends well below the added powder layer and that significant laser remelting takes place. A large amount of powder spatter is seen behind the keyhole with a lesser amount in front of it. Dark and streaked features in **Figure 4e** indicate fast-moving spatter particles. The shape and depth of the keyhole are akin to the keyholes observed under similar energy density conditions for laser scanning with [34] and without [41] a powder layer, *i.e*. laser welding.

Supplementary Videos 3 and **4** show the deposition of layer 5 in Samples C and D respectively, and also reveal prominent surface undulations and powder thickness variations. Notably, the video of Sample D shows significant porosity, characteristic of lack of fusion, at the end of the track.

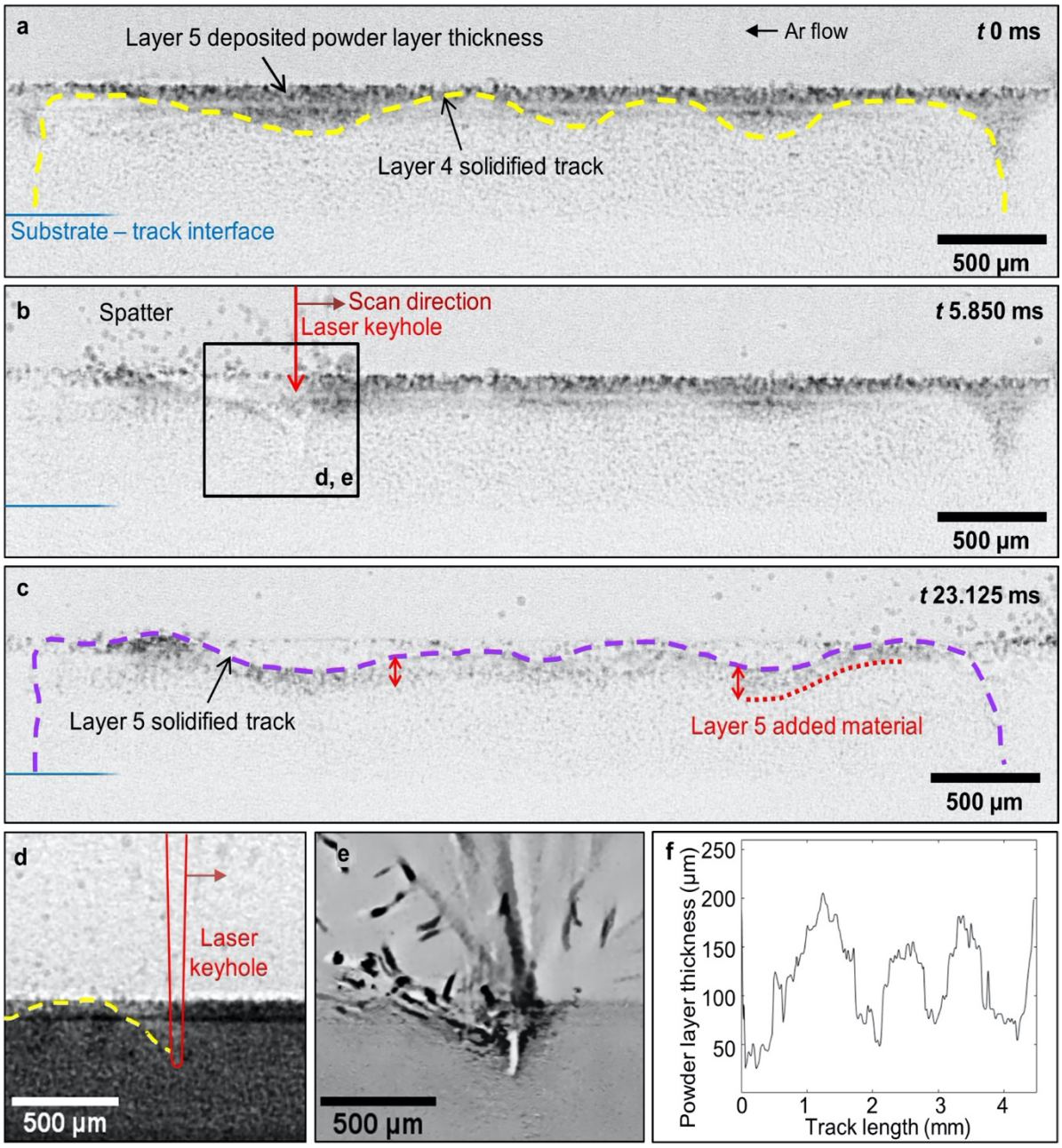

Figure 4**: (a)-(c) Background subtracted radiograph time series of Layer 5 melting in Sample B: **(a)** Track shape of prior 4 layers (yellow) with a deposited powder just before layer 5 is deposited. **(b)** ROI showing the formation of a deep keyhole depression during layer 5 melting (d-e). **(c)** Final track morphology of layer 5 (purple outline). **(d)** FFC radiograph of the laser-induced keyhole in layer 5. The red outline denotes the approximate position of the laser beam. **(e)** The keyhole shape is highlighted by locally averaging (d). **(f)** Graph showing the variation in powder layer thickness plot along the track length. Corresponding videos of the full track length melting with FFC and background subtraction (a-c) are shown in **Supplementary Video 5** and **6** respectively. Powder thickness variation plots of Samples A, C and D are shown in **Supplementary Figure 1.

3.2 Porosity analysis

μCT has been used to analyse pore shapes and sizes throughout all samples, to reveal overall trends in porosity. Pore formation mechanisms and interactions in multilayer builds are detailed in **3.3**. **Figure 5** shows μCT rendered images of the samples. The internal porosity has been highlighted by three colours, each representing a different D_{eq} size range. Pores of D_{eq} < 25 μm are termed small, those with 25 ≤ D_{eq} < 45 μm are termed mid-sized, and pores with D_{eq} ≥ 45 μm are termed large. The surface roughness visible on the sides and top of each sample was caused by semi-melted powder particles which adhered to the track but were not fully consolidated into the melt pool before solidification, see example in **Supplementary Figure 3**. **Table 2** shows the total number of pores of different size fractions and volume porosity for each condition. The percentage porosity was calculated using volume measurements from the μCT data; the methodology is in **Supplementary Information.**

In Sample A, substrate remelting must have taken place during the first build layer as the 6 pores observed were in the substrate. The largest volume porosity was measured in Sample B, in which the majority of large pores were observed at either end of the sample. **Figure 5** inset **(a)** illustrates the morphology of large irregularly shaped pores. The overall pore frequency histogram (below the μCT image for Sample B and C) shows a higher number of pores at each end of the track, and pore frequencies tend to be higher below the peaks in the deposition profile.

Sample C has about half the total volume porosity compared to Sample B, with reduced numbers of pores across all size ranges. The large pores are located towards one end of the track, where the solidified layer thickness is largest. Inset (b) shows a 'peanut' shaped large pore, in which two smaller pores appear to have coalesced. The pore frequency histogram reveals a correlation between the track height, and pore distribution, as more pores exist where the track is highest, which can be seen most clearly in **Figure 5** Sample C. The laser penetration depth into solidified track is lower than into the powder layer, so track peaks have a very thin layer of powder and substantial track remelting, whereas trough regions require

341 the laser to penetrate predominantly into powder. This suggests that when the track height is
342 higher, the laser penetration depth is not sufficient to remelt pores in the previous layer, and
343 could increase the overall pore volume. The variation in laser penetration depth of layer 5
344 melting can be seen in Supplementary Videos 2, 3, and 5.

345 The volume porosity in Sample D was measured to be similar to that of Sample A.
346 However, there are multiple regions showing poor layer cohesion, predominantly located at
347 the end of the track. Inset **(c)** shows evidence of a lack of fusion pore, which due to the nature
348 of single line scan tracks, propagated through the width of the sample. Although sample D has
349 around 2 % of the volume porosity compared with Sample B, this porosity analysis excludes
350 surface connected pores such as inset (c), and is thus an underestimation of the total volume
351 porosity, and care must be taken when comparing samples in this manner.

352

353 **Table 2:** Porosity quantification obtained from μCT data.

Sample ID	**Number of small pores**	**Number of mid-sized pores**	**Number of large pores**	**Total number of pores**	**Pore Volume** (μm^3) *****	**Percentage Porosity (%) ***
A	5	1	0	6	26 $x10^3$	0.0032
B	54	57	13	124	2322 $x10^3$	0.22
C	48	36	5	89	1126 $x10^3$	0.15
D	4	2	0	6	41 $x10^3$	0.0050

354 * The error range is from 2 – 6 %.

355

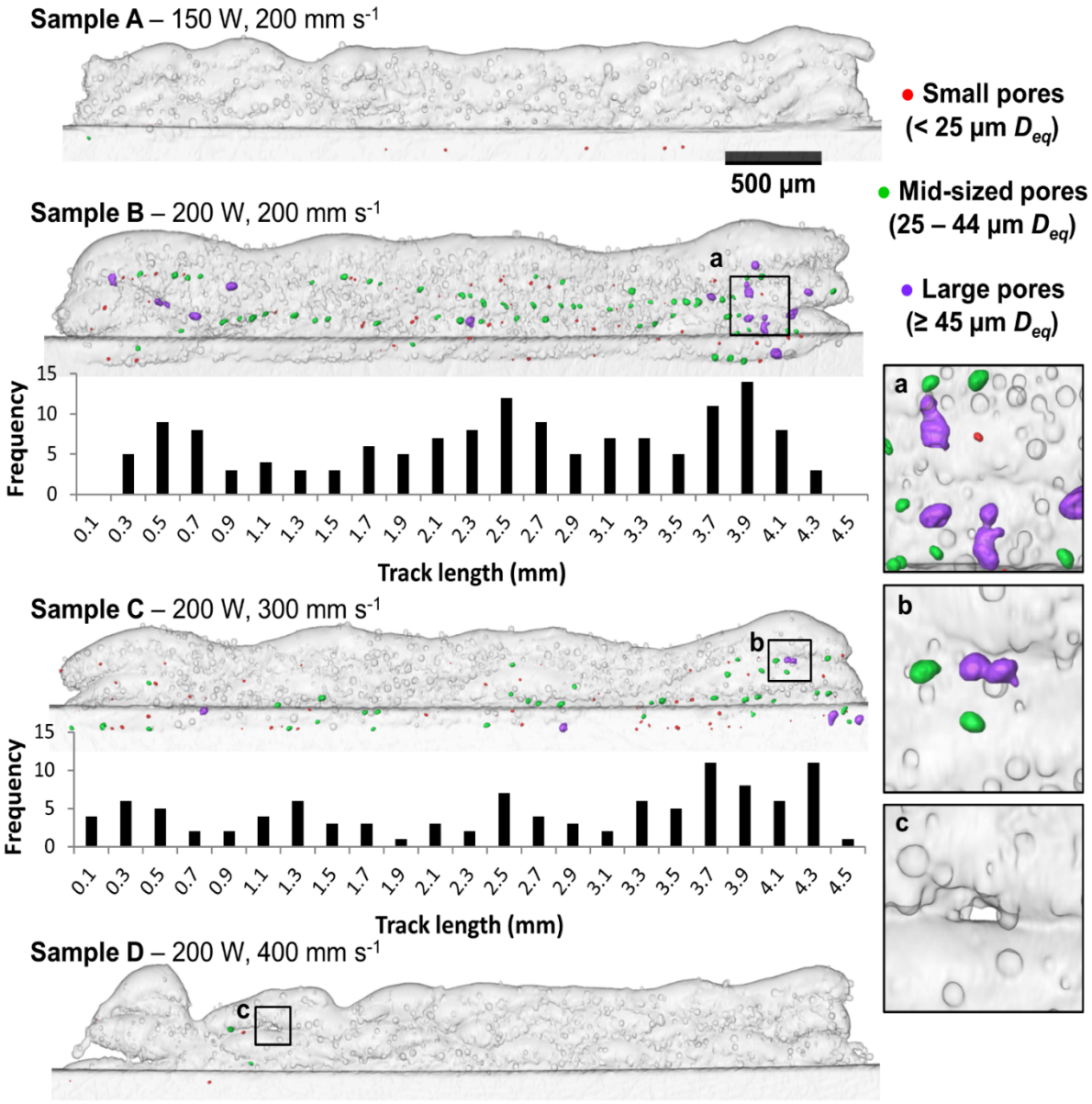

Figure 5: *3D rendered volumes from the reconstructed µCT scans highlighting pore size, distribution, and pore location. Pore frequency histograms with a bin size of 0.2 mm along the track length of Samples B and C. Insets* ***(a)*** *and* ***(b)*** *show large irregular pores. Inset* ***(c)*** *shows an interlayer pore. For interpretation of the colours in this figure, the reader is referred to the online version of this article.*

Figure 6 shows porosity measurements from the reconstructed µCT data, with pore volumes converted into D_{eq} values. The number fraction of internal pores measured in each sample is given in **Figure 6a**. Sample A has few pores, almost 70 % of which are in the 20 –

366 25 μm size range. An even range of small and mid-sized pores are evident in Samples B and
367 C. Sample D has very few pores but a similar number fraction of pores across the small and
368 mid-size ranges.

369 The pore volume fractions for each D_{eq} bin size is shown in **Figure 6b**, indicating their
370 contribution to the total overall volume porosity. Although Sample B and Sample C have a low
371 number of large pores, the plot shows that these contribute significantly to the overall volume
372 porosity. The highest number of pores in Sample C was small pores, however, the contribution
373 to volume porosity is low. The largest individual contribution being mid-sized pores; the
374 keyhole pores at the base of each melt layer. Sample D had a spike in pore volume from pores
375 in the range 30 – 35 μm (even though there is no spike in the number of pores) indicating that
376 fewer larger pores influence the volume porosity considerably more than many smaller sized
377 pores. Sample D had low overall pore volume because the methodology employed to analyse
378 the μCT data did not quantify the surface connected pores, such as that shown in **Figure 5**
379 inset (**c**).

380 **Figure 6c** shows the pore sphericity measurements in a scatter plot. The small pores
381 are typically close to spherical (sphericity value of 1). As the D_{eq} value increases, the spread
382 of the data also increases, showing pores to have a less uniform shape, with a minimum
383 sphericity of *ca.* 0.7 for large pores. The pores shown in **Figure 5** insets (**a**) and (**b**) are
384 representative of pores with low sphericity values. Sample B had the largest range in sphericity
385 values for all pore sizes of *ca.* 0.7 to 1.0. In Sample C, 96 % of pores had values ≥ 0.9, with a
386 minimum sphericity of 0.8. All pores in Samples A and D had high sphericity ≥ 0.96.
387

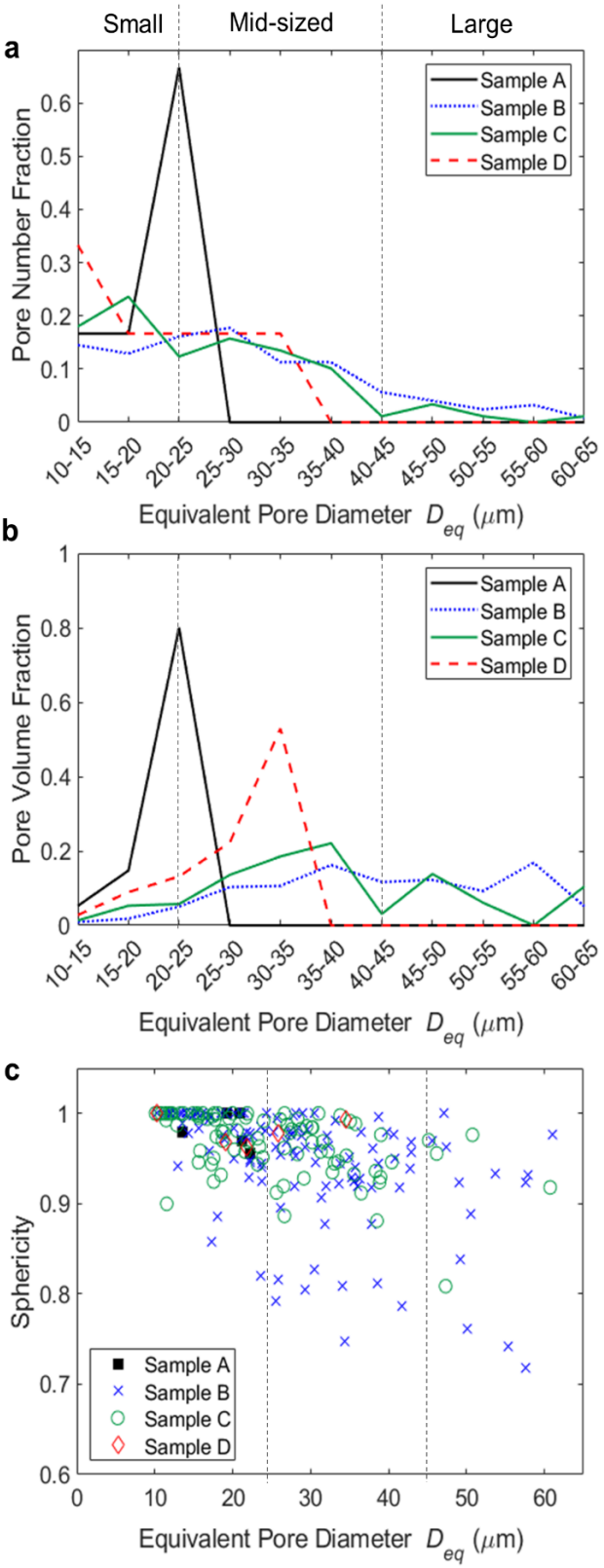

***Figure 6**: Measurements extracted from µCT analysis. **(a)** Pore number fraction plot, with dividing lines for small, medium and large pore size terms. **(b)** Volume fraction plot for all pores in each sample. **(c)** Scatter plot of pore sphericity for all measured pores.*

3.3 Keyhole melting and porosity formation observations

In the previous section, *ex situ* pore quantification has been reported. Through *in situ* X-ray radiography, it is possible to elucidate mechanisms by which the pores could have developed; described in this section. The melting of layer 1 in Sample C is shown in **Figure 7**, for a small region at the start of the melt track. **Figure 7a** shows a uniform powder layer of *ca.* 100 µm atop the substrate and **Figure 7b – d** show the evolution of the single layer melt track and keyhole pores in the substrate. As keyhole walls become unstable and collapse [34], pores form at the bottom of the keyhole. The insets in these figures (**b** – **d**) show locally averaged radiograph images of the keyhole shape and pore formation. **Figure 7e** and **f** show that these pores are retained inside the melt track, and an uneven track surface is formed upon solidification of the first layer.

Layer 2 melting and pore interactions in Sample C are shown in **Figure 8** for the same region of interest (ROI) as **Figure 7**. Details are shown in **Supplementary Videos 10** (full track) and **11** (cropped ROI), for layer 2. **Figure 8a** shows the full track length of layer 2 after melting, with the ROI highlighted for (**b – k**). **Figure 8b** shows a schematic (traced from radiographs) of layer 1, with the powder deposited for the next layer, just prior to melting.

Figure 8c – h show three different pore interactions that are observed to occur during multilayer laser melting and are described as follows: (i) the laser penetration depth of layer 2 melting is deep enough to interact with the solidified pore from the first layer, and the melt pool fills the void (**Figure 8c – d**, dotted yellow outline denotes a filled pore). (ii) The laser penetration depth is insufficient to fill the pre-existing pore with liquid metal (**Figure 8e** and **f**). This can be due to laser processing parameters, or in the case of Sample C, changes in track height along the length of the sample affect the depth of remelting, as described in **Figure 3**. (iii) The laser keyhole is unstable [34] and produces pores, in the same way to those in layer 1, and prior work [42,69]. These new voids may coalesce with existing pores to reduce interfacial energy in the melt pool, which increases their size. As the solidification rate is high,

these pores have not been able to rise to the surface and be removed before solidification (**Figure 8g – h**).

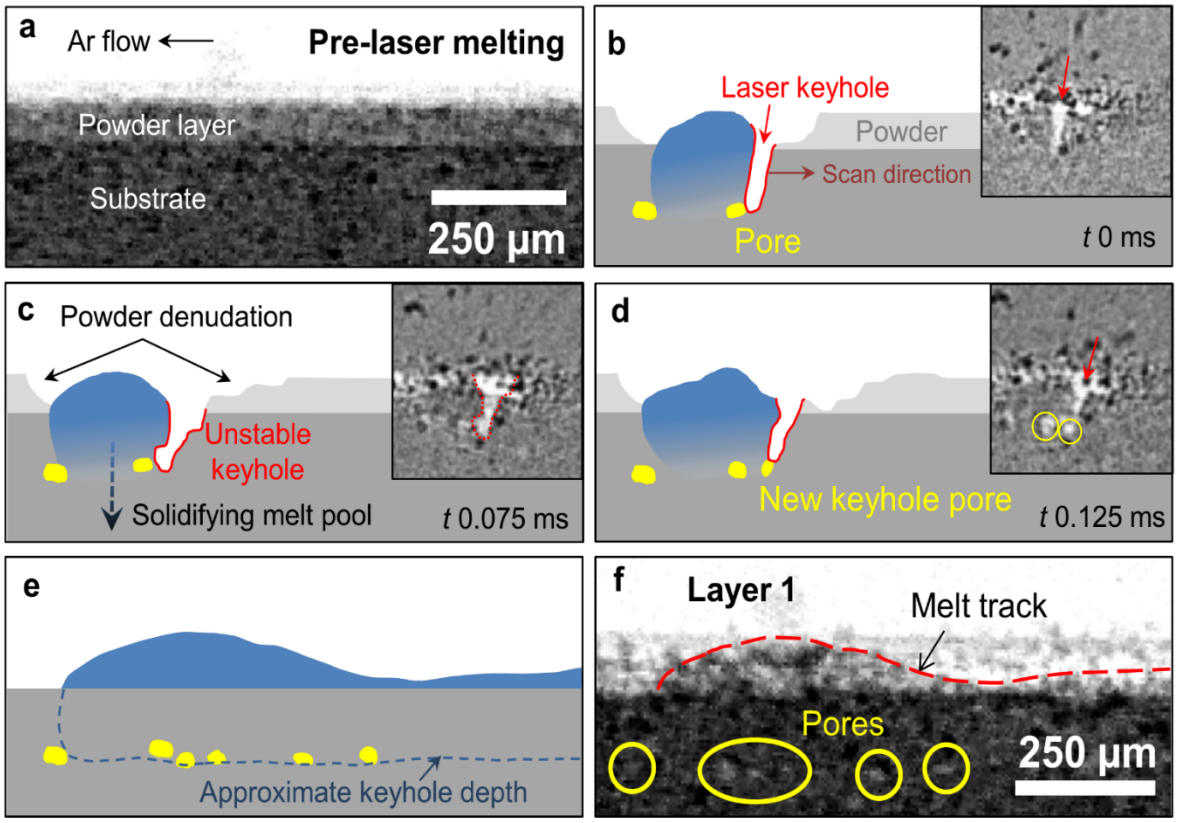

***Figure 7**: Observation of porosity formation in Sample C, layer 1. (**a**) Radiograph of substrate and powder prior to melting. Time series schematics (traced from the radiographs) and corresponding radiograph insets in **(b)** to **(d).** (**b**) Melt track (blue) with laser keyhole in the substrate plate (grey). (**c**) Keyhole walls become unstable. (**d**) A new pore is formed at the keyhole. (**e**) Pore positions after layer 1 melting where the blue dotted line shows the approximate keyhole depth. (**f**) Radiograph showing the position of the keyhole pores. See keyhole pore formation in **Supplementary Videos 7** (full track), **8** (cropped ROI), and **9** (locally averaged cropped ROI)**.** Insets in (**b – d**) are made by locally averaged radiograph images to highlight keyhole shape. **See Supplementary Videos 10 and 11**.*

In **Figure 8h,** the solidified layer 2 track is shown in blue, with solidified layer 1 outlined in the dashed red line. This shows that track remelting occurs and leads to a redistribution of material. **Figure 8i** is the final solidified layer 2 radiograph, with the μCT data as an overlay. It shows that the solidified pores observed remained in the sample. With high-resolution μCT scans (2.7 μm / voxel) relative to the synchrotron X-ray imaging (4.76 μm / pixel), we reveal additional pores in the samples which cannot be resolved in the X-ray radiograph. Pores produced in layers 3 – 5 are also visible in the μCT overlay.

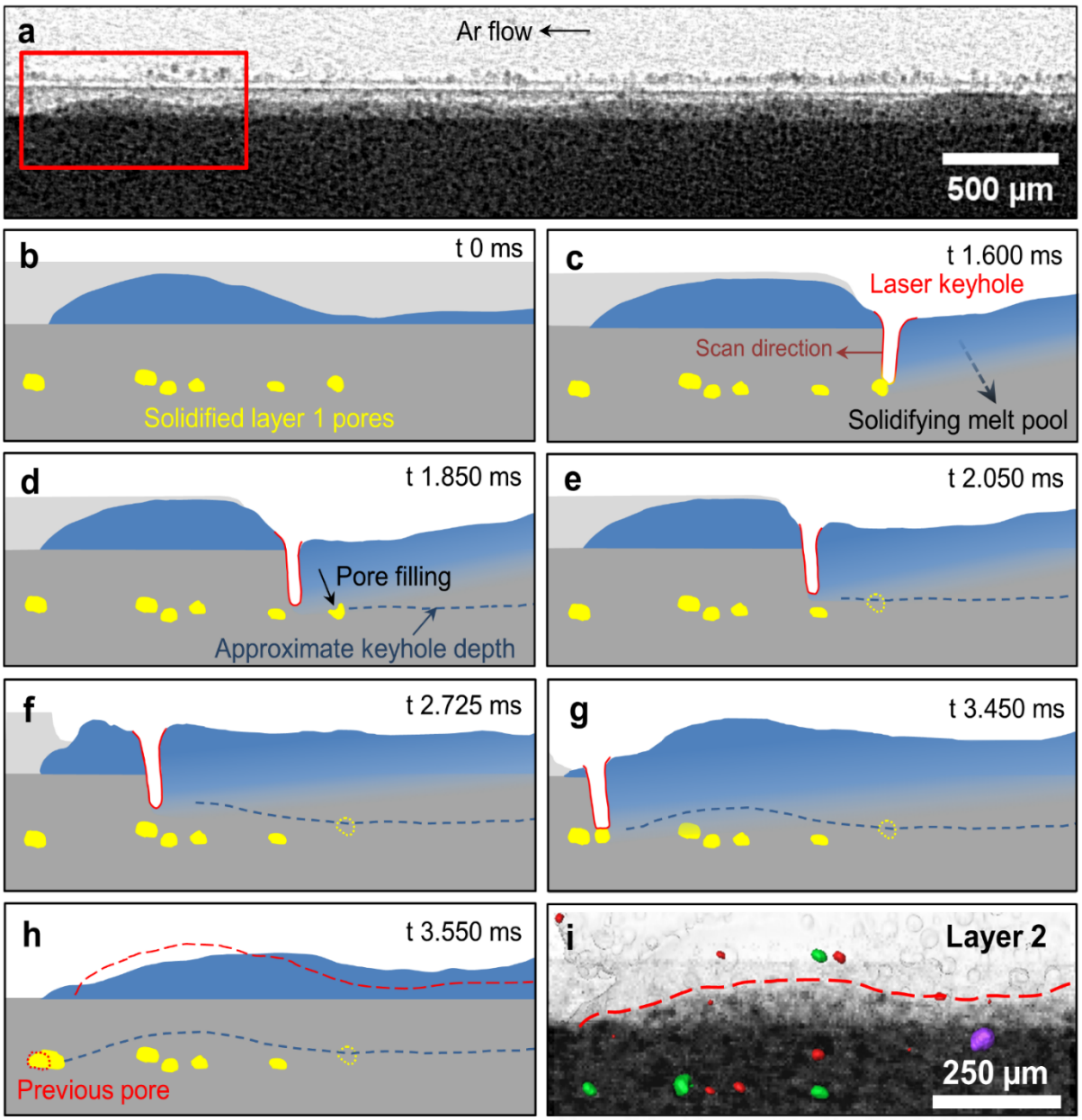

***Figure 8**: Schematic of porosity formation (traced from the radiographs) during deposition of the second layer in Sample C. **(a)** Radiograph of full track length after layer 2 melting, with the highlighted region of interest for (b – k). **(b)** Initial powder layer (100 µm) on the substrate, prior to laser melting. **(c – g)** Schematic of 3 laser interactions in multilayer melting. **(h)** Solidified layer 2 track; layer 1 outline shown in red. **(i)** Layer 2 final X-ray radiograph, with an overlay showing solidified pores in the sample from the µCT data. For the radiographs from which (b – h) are traced, please see **Supplementary Videos 10** and **11**.*

4. Discussion

4.1 Morphological development in multilayer tracks

Periodic undulations similar to those found in the present *in situ* study have also been observed in recent studies of the LPBF process, e.g. in thin-wall structures [70,71], in single line scan tracks [11,61] and in cubes [72]. They have also been seen in laser welding [73] and been modelled computationally [59]. The undulations, also referred to as humping [11], have been attributed to Marangoni flow in the melt pool and surface tension effects [70], mainly the Plateau-Rayleigh instability, which describes the break-up of fluid into discontinuous elements [74]. It is denoted as balling [4] when the effects are sufficiently extreme for LPBF tracks to become discontinuous.

A high length-to-width melt pool ratio would be expected to promote the Plateau-Rayleigh instability [11,61] and it has been reported that this increases the probability of such undulations developing [70]. It has also been observed that tracks produced under conditions of high *LED*, which increases melt pool length, produced more undulations [55,59,70]. However, in other studies, it has been found that decreasing the *LED* with a constant laser power led to a transition from a continuous track to surface undulations and to balling [55]. Evidently, there is a more complicated relationship between *LED* and formation of undulations, presumably because other process-related factors such as backward fluid flow in the molten pool [11] and recoil pressure [59] will play a role. In the present study, the range of *LED* values employed was not sufficiently great to provide further clarification. However, a notable feature from the *in situ* work is the observation in Sample A that the amplitude of undulations decreased as the number of layers increased, **Figure 3**. This could be related to the bidirectional melting strategy, but further research is necessary to confirm this.

The largest peak to trough distance observed was ca. 220 μm in Sample C, which has a substantial effect on layer remelting along the length of the track; as the keyhole depth was *ca.* 200 μm for these conditions in layer 5 (see Supplementary Video 5). This results in significant remelting of the previous layer at the wave peaks with little or none in the troughs.

The laser penetration depth itself also varied by 30 - 40 µm, going deeper in the troughs where it is melting power rather than prior solid track. Despite this deeper penetration at the troughs, in some areas the prior layer was sufficiently deep that that lack of fusion pores or unmelted powder between tracks was observed, such as those present in for Sample D, **Figure 5**. The effect of variable layer remelting is to directly influence the pore populations in multilayer samples, and this will be explored further in the following sections.

4.2 Gas Porosity

For GA powders, it is possible that gas trapped within the feedstock powder, typically argon [75], as a result of the manufacturing route can be entrained into the pool during melting [76], as well as retained soluble gases such as hydrogen [77]. In LPBF, hydrogen can also from several other sources, such as the decomposition of water vapour on the surface of the powder, or water vapour in the environmental chamber [78]. This is most prevalent in materials such as aluminium alloys [25] where hydrogen solubility increases with increasing temperature. Although this is not the case in titanium alloys, hydrogen has still been shown to cause porosity in welds [79–81], where at the liquidus temperature hydrogen is twice as soluble in the liquid as the solid (partition coefficient of *ca*. 0.5 [82]). Hence, hydrogen is rejected into the melt pool by the advancing solid-liquid interface and the melt becomes supersaturated. Hydrogen and other soluble gases will be swept along in the melt pool until the end of the track. When the laser is turned off at the end of the track, these soluble gases can become highly supersaturated as the liquid pool shrinks, and will either nucleate new pores, or diffuse into pores formed by the keyhole, stabilising or increasing their size. This may also happen all along the track, but to a lesser extent as the supersaturation will be less. This mechanism will be discussed later in greater detail. It is also possible that some of the small spherical pores will contain argon gas which is entrained from the environmental chamber when the keyhole pores form [4,33].

In some literature on the expected diameter of gas pores in additively manufactured materials, studies have classified any pores lower than 100 μm in diameter [29,83], or even between 100 μm and 300 μm [28] as gas pores. However, in the present study only those pores with D_{eq} approximately ≤ 30 μm had sphericity values close to 1 which is regarded as a strong indicator of a gas pore. Larger pores tended to have lower sphericity values and those visible on the radiograph images, measured to be *ca.* 40 – 60 μm in size, clearly formed via a keyhole mechanism. Therefore, it can be concluded that size alone cannot be used to determine the mechanism by which pores form and that further *in situ* studies are required to clarify this.

4.3 Keyhole pore formation

Supplementary Video 6 and **Figure 7** show keyhole pore formation over a 0.05 ms period. A keyhole is created, quickly distorted, and covered over by the unstable liquid metal above, resulting in a large entrapped pore. The final pore observed from this interaction is *ca.* 40 μm; similar to the size found in industrial practice [34,84]. This formation mechanism has also been explored computationally [4,33]. **Figure 5** shows that most irregular pores were found to be at the base of each melt track, and in the substrate for the initial layer. This supports their formation via the keyhole melting mechanism [10] and correlates with the stationary beam *in situ* experiments [34,36] in which the closure of a keyhole was seen to take *ca.* 0.05 ms. The decrease in sphericity (from 1.0 to 0.7) as the pore size increases implies that keyhole melting and metal vaporisation effects produced unstable voids [33,34], which were then trapped during solidification. The pores with low sphericity values may either have become distorted when trapped between dendrites [85], or when two pores are trapped as they coalesce (see **Figure 5** inset (**b**)). Large keyhole pores were most prevalent in Samples B and C and the number fraction of pores for each D_{eq} bin size show a similar trend, **Figure 6a**.

4.4 Keyhole-pore interactions in remelted layers

Lack of fusion pores are potentially detrimental features in AM components as they are generally non-uniform in shape [86], can contain unmelted powder particles [87], and can act as crack initiation sites. Therefore, based on the observations in this study, sufficient laser penetration depth, possibly through the keyhole mode of heating, can assist to ensure adequate fusion to the previous layer. A phase-field model of multilayer scanning [88] supports this, as a higher percentage of lack of fusion pores were observed when energy density was decreased. The effects of track balling led to pores, which were not remelted in subsequent layer addition, however in this work keyhole pores were not studied. In the present study, such lack of fusion features became more prominent in Samples C and D as the scan velocity was increased, and the depth of keyhole formation was expected to decrease. In Sample C, the layers at the ends of the track were insufficiently fused together. In Sample D, there were large areas of unfused material at the end of the track, as well as a lack of fusion pore mid-track, **Figure 5** inset (**c**). It can be estimated that the mid-track pore was *ca*. 60 µm long and the lack of fusion feature at the end of the track was *ca.* 450 µm long.

Whilst some remelting a previous layer is desirable, achieving this using keyholing may introduce keyhole pores at the interface between layers as shown in the *in situ* radiographs, and in the *ex situ* µCT reconstructions, **Figure 5**. However, the *in situ* radiographs, **Figure 8**, show that remelting can also be used advantageously, as large pores were eliminated from the track by a pore filling mechanism. Partial pore filling has also been observed previously [40]. Whether these pores were completely removed or redistributed as smaller pores [37] is unclear, as the spatial resolution of the radiographs is insufficient to confidently resolve pores with a diameter < 40 µm. Remelting was also seen to increase the size of one pore, **Figure 8h**, similar to that observed in overhang conditions [40], which is undesirable. The likelihood of this occurring could be related to the solidification rate, and whether pores have time to be filled by molten metal or rise to the surface of the melt before solidification. Therefore, careful control of layer remelting is an important factor to consider when selecting process conditions

554 in LPBF, as the multilayer *in situ* study has shown that complex interactions are taking place.
555 The selection of suitable process parameters is further complicated by the variations in powder
556 layer thickness, and consequently variable laser penetration to the previous layer. However,
557 a more in-depth analysis with a larger number of deposited layers would be necessary to
558 explore this. It must also be noted that this study only explored single melt track deposition,
559 and that some of the findings may not be applicable to typical depositions used in LPBF
560 employing multiple hatches and contours. However, this study is relevant to multilayer melting
561 and can be used to validate models, and hypotheses can be applied to hatched samples.
562

563 ## 4.5 Inhomogeneous pore distribution

564 The μCT results, **Figure 5**, clearly reveal that the large pores in Samples B and C form
565 primarily at the ends of each melt track and that this is also true of mid-size pores in Sample
566 C. Prior work has also observed a correlation between scan strategies and pore location
567 [22,23,30,72]. The irregular shapes of such pores are highlighted in the insets to this figure
568 and the time series radiographs in **Figure 8** provide clear mechanistic information of the role
569 of layer remelting in developing large irregular pores. Recently *in situ* methods [32] and
570 computational methods [5] have been used to study point pore formation during turning, *i.e.*
571 at the end of a track where the direction of travel changed. They concluded that pores form at
572 laser turn points due to the formation and subsequent collapse of a deep keyhole. However,
573 their powder-on-plate findings may not provide a full understanding of multilayer builds in
574 LPBF.

575 Our results suggest that both gas and keyhole pores are combined to form larger pores
576 during the melting and cooling of the track. The hypothesis is that firstly, the dissolved soluble
577 gases are swept along in the melt pool concentrating at the end of the track, similar to the
578 solute concentration that is observed in the Czochralski zone refining process [89]. Hydrogen
579 is a solute element in the molten alloy, with a partition coefficient k of ca. 0.5 [82]. During the
580 transformation from liquid to solid, hydrogen solubility decreases (halving for titanium), and

thus partitioning at the interface will concentrate dissolved hydrogen in the melt pool, sweeping solute elements to the end of the track. Normally, keyhole pores containing superheated metal vapour and a small amount of argon gas shrink as the melt pool cools. However, at the end of the track, the soluble gas (hydrogen) is concentrated by the sweeping (or Marangoni convection), and even further so as the pool solidifies at track end. This super-saturated gas could diffuse into the keyhole pores, increasing or maintaining their size.

The 'peanut' shape formed as two pores joined together in inset (**b**) indicates that the solidification process happened so rapidly that the void could not reshape into a sphere to reduce surface tension and was frozen as an irregular pore [30]. It is also possible that complex fluid flow could distort pore shapes. In agreement with a prior work [90], porosity minimisation at the ends of the track or turning points could be achieved via a reduction laser power in these areas to prevent keyhole porosity forming. The present work supports this as Sample A and B only differed in laser power (150 W and 200 W, respectively), but Sample A had 99 % less internal volume porosity. As can be seen from **Supplementary Videos 2** and **5**, the keyhole in Sample A is *ca.* 150 µm deep, while for Sample B the keyhole is *ca.* 250 µm, generating many more keyhole pores. Previous work similarly shows higher porosity percentage in higher energy conditions [91]. In large LPBF components, directionality, hatch strategy, and the depth of layer remelting will influence pore location and size, and all need to be carefully considered.

5. Conclusions

This study investigates the track formation and internal porosity during laser powder bed fusion of Ti-6Al-4V single track, multilayer builds using high speed *in situ* synchrotron imaging. The samples were further examined by *ex situ* µCT to further support our findings. The following conclusions have been drawn:

1. Undulations in the track surface were observed, which led to different depths of remelting along the track length in subsequent track, and thus different pore interactions

in multilayer builds. The deposited powder layer thickness changes as track height changes, decreasing the uniformity of multilayer components through this inconsistent remelting. This is an important factor which needs further investigation and consideration when selecting processing conditions.

2. There interactions were identified to occur during multilayer laser melting: (i) pores are remelted and the void is filled with molten metal; (ii) the laser penetration depth is not sufficient to fill the pore and they remain in the track; (iii) the laser keyhole is unstable and produces new pores, which can join to existing pores, increasing them in size.
3. Keyhole pore formation was quantified, illustrating how pore size varies as a function of build parameters (laser velocity and power), ranging from 10 – 60 µm, with those < 40 µm being detected ex situ with µCT. *In situ* keyhole pore formation was found to occur in a process taking under 0.05 ms, forming pores with a size *ca.* 30 – 60 µm, correlating well to prior *in situ* studies.
4. It is hypothesised that the formation of larger pores at the end of tracks is the result of the stabilising and growth of keyhole porosity by diffusion of supersaturated soluble gases (hydrogen) into these pores. This soluble gas is concentrated as the pool sweeps along the track due to the partition coefficient (k) of ca. 0.5. for hydrogen in titanium. Upon cooling at the end of track, the solubility rapidly decreases, and hydrogen diffuses into nearby pores.

6. Acknowledgements

The authors acknowledge financial support from the EPSRC MAPP Future Manufacturing Hub (EP/P006566/1, www.mapp.ac.uk); The Royal Academy of Engineering (CiET1819/10); Rolls-Royce Plc. through the Horizon 2020 Clean Sky 2 WP5.8.1 programmes (YC) and LS's Industrial Case studentship. We acknowledge the Research Complex at Harwell for use of facilities and thank the European Synchrotron Radiation Facility (ESRF) for providing the beamtime at beamline ID19 (MA-4061), and Elodie Bollier, Sam Tammas-Williams and

635 Samuel McDonald for their assistance in this beamtime. We thank Philip Holloway (Photron)
636 for lending us the FASTCAM SA-Z 2100K to enable this experiment. A special thanks to Prof.
637 Graham McCartney for all his help in revising the text and figures.

638 ## 7. Author contributions

639 PDL, LS, CLAL, and GB conceived the project. LS, YC and CLAL designed the experiments.
640 All authors performed the beamtime, except GB and JG. LS performed μCT, data analysis,
641 and results interpretation. LS, CLAL, and PDL led the results interpretation and paper writing,
642 with all authors contributing. JG performed the powder size distribution analysis.

643 ## 8. Data Availability

644 Representative samples of the research data are given in the figures (and supplementary data
645 – DOI if available). Due to their large size, other datasets generated and/or analysed during
646 this study are available from the corresponding author on reasonable request.

647 ## 9. Declaration of interest

648 The authors declare no competing financial interests.
649

10. References

[1] I. Gibson, D. Rosen, B. Stucker, Additive Manufacturing Technologies, 2015. https://doi.org/10.1007/978-1-4939-2113-3.

[2] W.E. Frazier, Metal additive manufacturing: A review, J. Mater. Eng. Perform. 23 (2014) 1917–1928. https://doi.org/10.1007/s11665-014-0958-z.

[3] M. Schmidt, M. Merklein, D. Bourell, D. Dimitrov, T. Hausotte, K. Wegener, L. Overmeyer, F. Vollertsen, G.N. Levy, Laser based additive manufacturing in industry and academia, CIRP Ann. 66 (2017) 561–583. https://doi.org/10.1016/j.cirp.2017.05.011.

[4] S.A. Khairallah, A.T. Anderson, A. Rubenchik, W.E. King, Laser powder-bed fusion additive manufacturing: Physics of complex melt flow and formation mechanisms of pores, spatter, and denudation zones, Acta Mater. 108 (2016) 36–45. https://doi.org/10.1016/j.actamat.2016.02.014.

[5] S.A. Khairallah, A.A. Martin, J.R.I. Lee, G. Guss, N.P. Calta, J.A. Hammons, M.H. Nielsen, K. Chaput, E. Schwalbach, M.N. Shah, M.G. Chapman, T.M. Willey, A.M. Rubenchik, A.T. Anderson, Y.M. Wang, M.J. Matthews, W.E. King, Controlling interdependent meso-nanosecond dynamics and defect generation in metal 3D printing, Science (80-.). 368 (2020) 660–665. https://doi.org/10.1126/science.aay7830.

[6] C. Qiu, S. Yue, N.J.E.E. Adkins, M. Ward, H. Hassanin, P.D. Lee, P.J. Withers, M.M. Attallah, Influence of processing conditions on strut structure and compressive properties of cellular lattice structures fabricated by selective laser melting, Mater. Sci. Eng. A. 628 (2015) 188–197. https://doi.org/10.1016/j.msea.2015.01.031.

[7] T.B. Sercombe, X. Xu, V.J. Challis, R. Green, S. Yue, Z. Zhang, P.D. Lee, Failure modes in high strength and stiffness to weight scaffolds produced by Selective Laser Melting, Mater. Des. 67 (2015) 501–508. https://doi.org/10.1016/j.matdes.2014.10.063.

[8] I. Yadroitsev, A. Gusarov, I. Yadroitsava, I. Smurov, Single track formation in selective laser melting of metal powders, J. Mater. Process. Technol. 210 (2010) 1624–1631. https://doi.org/10.1016/j.jmatprotec.2010.05.010.

[9] C. Qiu, C. Panwisawas, M. Ward, H.C. Basoalto, J.W. Brooks, M.M. Attallah, On the role of melt flow into the surface structure and porosity development during selective laser melting, Acta Mater. 96 (2015) 72–79. https://doi.org/10.1016/j.actamat.2015.06.004.

[10] W.E. King, H.D. Barth, V.M. Castillo, G.F. Gallegos, J.W. Gibbs, D.E. Hahn, C. Kamath, A.M. Rubenchik, Observation of keyhole-mode laser melting in laser powder-

686 bed fusion additive manufacturing, J. Mater. Process. Technol. 214 (2014) 2915–
687 2925. https://doi.org/10.1016/j.jmatprotec.2014.06.005.
688 [11] V. Gunenthiram, P. Peyre, M. Schneider, M. Dal, F. Coste, R. Fabbro, Analysis of
689 laser – melt pool – powder bed interaction during the selective laser melting of a
690 stainless steel, J. Laser Appl. 2 (2017).
691 [12] D.D. Gu, W. Meiners, K. Wissenbach, R. Poprawe, Laser additive manufacturing of
692 metallic components: materials, processes and mechanisms, Int. Mater. Rev. 57
693 (2012) 133–164. https://doi.org/10.1179/1743280411Y.0000000014.
694 [13] M. Taheri Andani, R. Dehghani, M.R. Karamooz-Ravari, R. Mirzaeifar, J. Ni, A study
695 on the effect of energy input on spatter particles creation during selective laser
696 melting process, Addit. Manuf. 20 (2018) 33–43.
697 https://doi.org/10.1016/j.addma.2017.12.009.
698 [14] M. Thomas, G.J. Baxter, I. Todd, Normalised model-based processing diagrams for
699 additive layer manufacture of engineering alloys, Acta Mater. 108 (2016) 26–35.
700 https://doi.org/10.1016/j.actamat.2016.02.025.
701 [15] R. Li, J. Liu, Y. Shi, L. Wang, W. Jiang, Balling behavior of stainless steel and nickel
702 powder during selective laser melting process, Int. J. Adv. Manuf. Technol. 59 (2012)
703 1025–1035. https://doi.org/10.1007/s00170-011-3566-1.
704 [16] R. Cunningham, S.P. Narra, C. Montgomery, J. Beuth, A.D. Rollett, Synchrotron-
705 Based X-ray Microtomography Characterization of the Effect of Processing Variables
706 on Porosity Formation in Laser Power-Bed Additive Manufacturing of Ti-6Al-4V, Jom.
707 69 (2017) 479–484. https://doi.org/10.1007/s11837-016-2234-1.
708 [17] D. Gu, Y. Shen, Effects of processing parameters on consolidation and microstructure
709 of W-Cu components by DMLS, J. Alloys Compd. 473 (2009) 107–115.
710 https://doi.org/10.1016/j.jallcom.2008.05.065.
711 [18] L. Thijs, F. Verhaeghe, T. Craeghs, J. Van Humbeeck, J.P. Kruth, A study of the
712 microstructural evolution during selective laser melting of Ti-6Al-4V, Acta Mater. 58
713 (2010) 3303–3312. https://doi.org/10.1016/j.actamat.2010.02.004.
714 [19] B. Vrancken, L. Thijs, J.P. Kruth, J. Van Humbeeck, Microstructure and mechanical
715 properties of a novel β titanium metallic composite by selective laser melting, Acta
716 Mater. 68 (2014) 150–158. https://doi.org/10.1016/j.actamat.2014.01.018.
717 [20] F. Léonard, S. Tammas-Williams, I. Todd, CT for Additive Manufacturing Process
718 Characterisation: Assessment of melt strategies on defect population, 6th Conf. Ind.
719 Comput. Tomogr. (2016) 8. www.3dct.at.
720 [21] W.J. Sames, F.A. List, S. Pannala, R.R. Dehoff, S.S. Babu, The metallurgy and
721 processing science of metal additive manufacturing, Int. Mater. Rev. 61 (2016) 315–
722 360. https://doi.org/10.1080/09506608.2015.1116649.

[22] C. Pirozzi, S. Franchitti, R. Borrelli, G. Diodati, G. Vattasso, Experimental Study on the Porosity of Electron Beam Melting-Manufactured Ti6Al4V, J. Mater. Eng. Perform. 28 (2019) 2649–2660. https://doi.org/10.1007/s11665-019-04038-7.

[23] H. Galarraga, D.A. Lados, R.R. Dehoff, M.M. Kirka, P. Nandwana, Effects of the microstructure and porosity on properties of Ti-6Al-4V ELI alloy fabricated by electron beam melting (EBM), Addit. Manuf. 10 (2016) 47–57. https://doi.org/10.1016/j.addma.2016.02.003.

[24] J.H. Tan, W.L.E. Wong, K.W. Dalgarno, An overview of powder granulometry on feedstock and part performance in the selective laser melting process, Addit. Manuf. 18 (2017) 228–255. https://doi.org/10.1016/j.addma.2017.10.011.

[25] P.D. Lee, J.D. Hunt, Measuring the nucleation of hydrogen porosity during the solidification of aluminium-copper alloys, Scr. Mater. 36 (1997) 399–404. https://doi.org/10.1016/S1359-6462(96)00411-3.

[26] P.D. Lee, A. Chirazi, D. See, Modeling microporosity in aluminum-silicon alloys: A review, J. Light Met. 1 (2001) 15–30. https://doi.org/10.1016/S1471-5317(00)00003-1.

[27] A. Haboudou, P. Peyre, A.B. Vannes, G. Peix, Reduction of porosity content generated during Nd: YAG laser welding of A356 and AA5083 aluminium alloys, Mater. Sci. Eng. A. 363 (2003) 40–52. https://doi.org/10.1016/S0921-5093(03)00637-3.

[28] J.L. Huang, N. Warnken, J.C. Gebelin, M. Strangwood, R.C. Reed, On the mechanism of porosity formation during welding of titanium alloys, Acta Mater. 60 (2012) 3215–3225. https://doi.org/10.1016/j.actamat.2012.02.035.

[29] N.T. Aboulkhair, N.M. Everitt, I. Ashcroft, C. Tuck, Reducing porosity in AlSi10Mg parts processed by selective laser melting, Addit. Manuf. 1 (2014) 77–86. https://doi.org/10.1016/j.addma.2014.08.001.

[30] S. Tammas-Williams, H. Zhao, F. Léonard, F. Derguti, I. Todd, P.B. Prangnell, XCT analysis of the influence of melt strategies on defect population in Ti-6Al-4V components manufactured by Selective Electron Beam Melting, Mater. Charact. 102 (2015) 47–61. https://doi.org/10.1016/j.matchar.2015.02.008.

[31] G.K.L. Ng, A.E.W. Jarfors, G. Bi, H.Y. Zheng, Porosity formation and gas bubble retention in laser metal deposition, Appl. Phys. A Mater. Sci. Process. 97 (2009) 641–649. https://doi.org/10.1007/s00339-009-5266-3.

[32] A.A. Martin, N.P. Calta, J.A. Hammons, S.A. Khairallah, M.H. Nielsen, R.M. Shuttlesworth, N. Sinclair, M.J. Matthews, J.R. Jeffries, T.M. Willey, J.R.I. Lee, Ultrafast dynamics of laser-metal interactions in additive manufacturing alloys captured by in situ X-ray imaging, Mater. Today Adv. 1 (2019) 100002. https://doi.org/10.1016/j.mtadv.2019.01.001.

[33] C. Panwisawas, B. Perumal, R.M. Ward, N. Turner, R.P. Turner, J.W. Brooks, H.C. Basoalto, Keyhole formation and thermal fluid flow-induced porosity during laser fusion welding in titanium alloys: Experimental and modelling, Acta Mater. 126 (2017) 251–263. https://doi.org/10.1016/j.actamat.2016.12.062.

[34] R. Cunningham, C. Zhao, N. Parab, C. Kantzos, J. Pauza, K. Fezzaa, T. Sun, A.D. Rollett, Keyhole threshold and morphology in laser melting revealed by ultrahigh-speed x-ray imaging, Science (80-.). 363 (2019) 849–852. https://doi.org/10.1126/science.aav4687.

[35] M. Zhang, G. Chen, Y. Zhou, S. Li, Direct observation of keyhole characteristics in deep penetration laser welding with a 10 kW fiber laser, Opt. Express. 21 (2013) 19997. https://doi.org/10.1364/oe.21.019997.

[36] C. Zhao, K. Fezzaa, R.W. Cunningham, H. Wen, F. De Carlo, L. Chen, A.D. Rollett, T. Sun, Real-time monitoring of laser powder bed fusion process using high-speed X-ray imaging and diffraction, Sci. Rep. 7 (2017) 3602. https://doi.org/10.1038/s41598-017-03761-2.

[37] C.L.A. Leung, S. Marussi, R.C. Atwood, P.D. Lee, M. Towrie, P.J. Withers, In situ X-ray imaging of defect and molten pool dynamics in laser additive manufacturing, Nat. Commun. 9 (2018) 1–9. https://doi.org/10.1038/s41467-018-03734-7.

[38] T. Sun, Probing Ultrafast Dynamics in Laser Powder Bed Fusion Using High-Speed X-Ray Imaging: A Review of Research at the Advanced Photon Source, Jom. 72 (2020) 999–1008. https://doi.org/10.1007/s11837-020-04015-9.

[39] Q. Guo, C. Zhao, L.I. Escano, Z. Young, L. Xiong, K. Fezzaa, W. Everhart, B. Brown, T. Sun, L. Chen, Transient dynamics of powder spattering in laser powder bed fusion additive manufacturing process revealed by in-situ high-speed high-energy x-ray imaging, Acta Mater. 151 (2018) 169–180. https://doi.org/10.1016/j.actamat.2018.03.036.

[40] C.L.A. Leung, S. Marussi, M. Towrie, R.C. Atwood, P.J. Withers, P.D. Lee, The effect of powder oxidation on defect formation in laser additive manufacturing, Acta Mater. 166 (2019) 294–305. https://doi.org/10.1016/J.ACTAMAT.2018.12.027.

[41] N.D. Parab, C. Zhao, R. Cunningham, L.I. Escano, K. Fezzaa, W. Everhart, A.D. Rollett, L. Chen, T. Sun, Ultrafast X-ray imaging of laser–metal additive manufacturing processes, J. Synchrotron Radiat. 25 (2018) 1467–1477. https://doi.org/10.1107/s1600577518009554.

[42] A. Bobel, L.G. Hector, I. Chelladurai, A.K. Sachdev, T. Brown, W.A. Poling, R. Kubic, B. Gould, C. Zhao, N. Parab, A. Greco, T. Sun, In situ synchrotron X-ray imaging of 4140 steel laser powder bed fusion, Materialia. 6 (2019) 100306. https://doi.org/10.1016/J.MTLA.2019.100306.

[43] N.P. Calta, J. Wang, A.M. Kiss, A.A. Martin, P.J. Depond, G.M. Guss, V. Thampy, A.Y. Fong, J.N. Weker, K.H. Stone, C.J. Tassone, M.J. Kramer, M.F. Toney, A. Van Buuren, M.J. Matthews, An instrument for in situ time-resolved X-ray imaging and diffraction of laser powder bed fusion additive manufacturing processes, Rev. Sci. Instrum. 89 (2018). https://doi.org/10.1063/1.5017236.

[44] N.D. Parab, C. Zhao, R. Cunningham, L.I. Escano, B. Gould, S. Wolff, Q. Guo, L. Xiong, C. Kantzos, J. Pauza, K. Fezzaa, A. Greco, A. Rollett, L. Chen, T. Sun, High-speed Synchrotron X-ray Imaging of Laser Powder Bed Fusion Process, Synchrotron Radiat. News. 32 (2019) 4–8. https://doi.org/10.1080/08940886.2019.1582280.

[45] S. Shevchik, T. Le-Quang, B. Meylan, F.V. Farahani, M.P. Olbinado, A. Rack, G. Masinelli, C. Leinenbach, K. Wasmer, Supervised deep learning for real-time quality monitoring of laser welding with X-ray radiographic guidance, Sci. Rep. 10 (2020) 3389. https://doi.org/10.1038/s41598-020-60294-x.

[46] A.M. Kiss, A.Y. Fong, N.P. Calta, V. Thampy, A.A. Martin, P.J. Depond, J. Wang, M.J. Matthews, R.T. Ott, C.J. Tassone, K.H. Stone, M.J. Kramer, A. van Buuren, M.F. Toney, J. Nelson Weker, Laser-Induced Keyhole Defect Dynamics during Metal Additive Manufacturing, Adv. Eng. Mater. 21 (2019) 1–7. https://doi.org/10.1002/adem.201900455.

[47] S.M.H. Hojjatzadeh, N.D. Parab, W. Yan, Q. Guo, L. Xiong, C. Zhao, M. Qu, L.I. Escano, X. Xiao, K. Fezzaa, W. Everhart, T. Sun, L. Chen, Pore elimination mechanisms during 3D printing of metals, Nat. Commun. 10 (2019) 3088. https://doi.org/10.1038/s41467-019-10973-9.

[48] C.L.A. Leung, R. Tosi, E. Muzangaza, S. Nonni, P.J. Withers, P.D. Lee, Effect of preheating on the thermal, microstructural and mechanical properties of selective electron beam melted Ti-6Al-4V components, Mater. Des. 174 (2019) 107792. https://doi.org/10.1016/j.matdes.2019.107792.

[49] T.B. Kim, S. Yue, Z. Zhang, E. Jones, J.R. Jones, P.D. Lee, Additive manufactured porous titanium structures: Through-process quantification of pore and strut networks, J. Mater. Process. Technol. 214 (2014) 2706–2715. https://doi.org/10.1016/j.jmatprotec.2014.05.006.

[50] S. Yue, P.D. Lee, G. Poologasundarampillai, J.R. Jones, Evaluation of 3-D bioactive glass scaffolds dissolution in a perfusion flow system with X-ray microtomography, Acta Biomater. 7 (2011) 2637–2643. https://doi.org/10.1016/j.actbio.2011.02.009.

[51] C.L.A. Leung, S. Marussi, M. Towrie, J. del Val Garcia, R.C. Atwood, A.J. Bodey, J.R. Jones, P.J. Withers, P.D. Lee, Laser-matter interactions in additive manufacturing of stainless steel SS316L and 13-93 bioactive glass revealed by in situ X-ray imaging, Addit. Manuf. 24 (2018) 647–657. https://doi.org/10.1016/j.addma.2018.08.025.

[52] V. Bhavar, P. Kattire, V. Patil, S. Khot, K. Gujar, R. Singh, A Review on Powder Bed Fusion Technology of Metal Additive Manufacturing, 4th Int. Conf. Exhib. Addit. Manuf. Technol. (2014).
[53] W. Shi, P. Wang, Y. Liu, Y. Hou, G. Han, Properties of 316L formed by a 400 W power laser Selective Laser Melting with 250 μm layer thickness, Powder Technol. 360 (2020) 151–164. https://doi.org/10.1016/j.powtec.2019.09.059.
[54] S. Wang, Y. Liu, W. Shi, B. Qi, J. Yang, F. Zhang, D. Han, Y. Ma, Research on high layer thickness fabricated of 316L by selective laser melting, Materials (Basel). 10 (2017). https://doi.org/10.3390/ma10091055.
[55] U. Scipioni Bertoli, A.J. Wolfer, M.J. Matthews, J.P.R. Delplanque, J.M. Schoenung, On the limitations of Volumetric Energy Density as a design parameter for Selective Laser Melting, Mater. Des. 113 (2017) 331–340. https://doi.org/10.1016/j.matdes.2016.10.037.
[56] D.D. Gu, Y.F. Shen, J.L. Yang, Y. Wang, Effects of processing parameters on direct laser sintering of multicomponent Cu based metal powder, Mater. Sci. Technol. 22 (2006) 1449–1455. https://doi.org/10.1179/174328406X111057.
[57] D. Wang, C. Song, Y. Yang, Y. Bai, Investigation of crystal growth mechanism during selective laser melting and mechanical property characterization of 316L stainless steel parts, Mater. Des. 100 (2016) 291–299. https://doi.org/10.1016/j.matdes.2016.03.111.
[58] O. Andreau, I. Koutiri, P. Peyre, J.D. Penot, N. Saintier, E. Pessard, T. De Terris, C. Dupuy, T. Baudin, Texture control of 316L parts by modulation of the melt pool morphology in selective laser melting, J. Mater. Process. Technol. 264 (2019) 21–31. https://doi.org/10.1016/j.jmatprotec.2018.08.049.
[59] C. Tang, K.Q. Le, C.H. Wong, Physics of humping formation in laser powder bed fusion, Int. J. Heat Mass Transf. 149 (2020) 119172. https://doi.org/10.1016/j.ijheatmasstransfer.2019.119172.
[60] H. Zheng, H. Li, L. Lang, S. Gong, Y. Ge, Effects of scan speed on vapor plume behavior and spatter generation in laser powder bed fusion additive manufacturing, J. Manuf. Process. 36 (2018) 60–67. https://doi.org/10.1016/j.jmapro.2018.09.011.
[61] V. Gunenthiram, P. Peyre, M. Schneider, M. Dal, F. Coste, I. Koutiri, R. Fabbro, Experimental analysis of spatter generation and melt-pool behavior during the powder bed laser beam melting process, J. Mater. Process. Technol. 251 (2018) 376–386. https://doi.org/10.1016/j.jmatprotec.2017.08.012.
[62] N. Kouraytem, X. Li, R. Cunningham, C. Zhao, N. Parab, T. Sun, A.D. Rollett, A.D. Spear, W. Tan, Effect of Laser-Matter Interaction on Molten Pool Flow and Keyhole Dynamics, Phys. Rev. Appl. 11 (2019) 064054.

https://doi.org/10.1103/PhysRevApplied.11.064054.
[63] M.P. Olbinado, X. Just, J.-L. Gelet, P. Lhuissier, M. Scheel, P. Vagovic, T. Sato, R. Graceffa, J. Schulz, A. Mancuso, J. Morse, A. Rack, MHz frame rate hard X-ray phase-contrast imaging using synchrotron radiation, Opt. Express. 25 (2017) 13857. https://doi.org/10.1364/oe.25.013857.
[64] H. Wadell, Volume, shape, and roundness of quartz particles, J. Geol. 43 (1935) 250–280.
[65] Thermo Scientific Avizo Software 9 User 's Guide, (n.d.).
[66] J. Schindelin, I. Arganda-Carreras, E. Frise, V. Kaynig, M. Longair, T. Pietzsch, S. Preibisch, C. Rueden, S. Saalfeld, B. Schmid, J.Y. Tinevez, D.J. White, V. Hartenstein, K. Eliceiri, P. Tomancak, A. Cardona, Fiji: An open-source platform for biological-image analysis, Nat. Methods. 9 (2012) 676–682. https://doi.org/10.1038/nmeth.2019.
[67] P. Bidare, R.R.J. Maier, R.J. Beck, J.D. Shephard, A.J. Moore, An open-architecture metal powder bed fusion system for in-situ process measurements, Addit. Manuf. 16 (2017) 177–185. https://doi.org/10.1016/j.addma.2017.06.007.
[68] P. Bidare, I. Bitharas, R.M. Ward, M.M. Attallah, A.J. Moore, Fluid and particle dynamics in laser powder bed fusion, Acta Mater. 142 (2018) 107–120. https://doi.org/10.1016/j.actamat.2017.09.051.
[69] Y. Chen, S.J. Clark, C. Lun, A. Leung, L. Sinclair, S. Marussi, M.P. Olbinado, E. Boller, A. Rack, I. Todd, P.D. Lee, In-situ Synchrotron imaging of keyhole mode multi-layer laser powder bed fusion additive manufacturing, Appl. Mater. Today. 20 (2020) 100650. https://doi.org/10.1016/j.apmt.2020.100650.
[70] U. Scipioni Bertoli, G. Guss, S. Wu, M.J. Matthews, J.M. Schoenung, In-situ characterization of laser-powder interaction and cooling rates through high-speed imaging of powder bed fusion additive manufacturing, Mater. Des. 135 (2017) 385–396. https://doi.org/10.1016/j.matdes.2017.09.044.
[71] I. Yadroitsev, P. Bertrand, Use of track/layer morphology to develop functional parts by selective laser melting, J. Laser …. 25 (2013) 1–7. https://doi.org/10.2351/1.4811838.
[72] P.J. DePond, G. Guss, S. Ly, N.P. Calta, D. Deane, S. Khairallah, M.J. Matthews, In situ measurements of layer roughness during laser powder bed fusion additive manufacturing using low coherence scanning interferometry, Mater. Des. 154 (2018) 347–359. https://doi.org/10.1016/j.matdes.2018.05.050.
[73] M. Seiler, A. Patschger, J. Bliedtner, Investigations of welding instabilities and weld seam formation during laser microwelding of ultrathin metal sheets, J. Laser Appl. 28 (2016) 022417. https://doi.org/10.2351/1.4944446.

[74] J. Eggers, Nonlinear dynamics and breakup of free-surface flows, Rev. Mod. Phys. 69 (1997) 865–930. https://doi.org/10.1103/RevModPhys.69.865.
[75] P. Sun, Z.Z. Fang, Y. Zhang, Y. Xia, Review of the Methods for Production of Spherical Ti and Ti Alloy Powder, JOM. 69 (2017) 1853–1860. https://doi.org/10.1007/s11837-017-2513-5.
[76] M.N. Ahsan, R. Bradley, A.J. Pinkerton, Microcomputed tomography analysis of intralayer porosity generation in laser direct metal deposition and its causes, J. Laser Appl. 23 (2011) 022009. https://doi.org/10.2351/1.3582311.
[77] C. Zhong, J. Chen, S. Linnenbrink, A. Gasser, S. Sui, R. Poprawe, A comparative study of Inconel 718 formed by High Deposition Rate Laser Metal Deposition with GA powder and PREP powder, Mater. Des. 107 (2016) 386–392. https://doi.org/10.1016/j.matdes.2016.06.037.
[78] I.E. Anderson, E.M.H. White, R. Dehoff, Feedstock powder processing research needs for additive manufacturing development, Curr. Opin. Solid State Mater. Sci. (2018) 1–8. https://doi.org/10.1016/j.cossms.2018.01.002.
[79] T. Mohandas, D. Banerjee, V. V. Kutumba Rao, Fusion zone microstructure and porosity in electron beam welds of an α+β titanium alloy, Metall. Mater. Trans. A. 30 (1999) 789–798. https://doi.org/10.1007/s11661-999-0071-3.
[80] T.R. Muth, Y. Yamamoto, D.A. Frederick, C.I. Contescu, W. Chen, Y.C. Lim, W.H. Peter, Z. Feng, Causal factors of weld porosity in gas tungsten arc welding of powder-metallurgy-produced titanium alloys, Jom. 65 (2013) 643–651. https://doi.org/10.1007/s11837-013-0592-5.
[81] J. Huang, N. Warnken, J.C. Gebelin, M. Strangwood, R.C. Reed, Hydrogen transport and rationalization of porosity formation during welding of titanium alloys, Metall. Mater. Trans. A Phys. Metall. Mater. Sci. 43 (2012) 582–591. https://doi.org/10.1007/s11661-011-0867-9.
[82] C.E. Cross, D. Eliezer, T. Böllinghaus, The Role of Hydrogen in Titanium Alloy Weldments, 22nd Int. Titan. Conf. Titanium A (2006) 26–31.
[83] S. Liu, Y.C. Shin, Additive manufacturing of Ti6Al4V alloy: A review, Mater. Des. 164 (2019) 107552. https://doi.org/10.1016/j.matdes.2018.107552.
[84] B. Shen, H. Li, S. Liu, J. Zou, S. Shen, Y. Wang, T. Zhang, D. Zhang, Y. Chen, H. Qi, Influence of laser post-processing on pore evolution of Ti–6Al–4V alloy by laser powder bed fusion, J. Alloys Compd. 818 (2020) 152845. https://doi.org/10.1016/j.jallcom.2019.152845.
[85] P.D. Lee, J.D. Hunt, Hydrogen porosity in directional solidified aluminium-copper alloys: In situ observation, Acta Mater. 45 (1997) 4155–4169. https://doi.org/10.1016/S1359-6454(97)00081-5.

945 [86] W.J. Sames, F. Medina, W.H. Peter, S.S. Babu, R.R. Dehoff, Effect of process control
946 and powder quality on inconel 718 produced using electron beam melting, 8th Int.
947 Symp. Superalloy 718 Deriv. 2014. (2014) 409–423.
948 https://doi.org/10.1002/9781119016854.ch32.
949 [87] H. Gong, K. Rafi, H. Gu, T. Starr, B. Stucker, Analysis of defect generation in Ti-6Al-
950 4V parts made using powder bed fusion additive manufacturing processes, Addit.
951 Manuf. 1 (2014) 87–98. https://doi.org/10.1016/j.addma.2014.08.002.
952 [88] L. Lu, N. Sridhar, Y. Zhang, Acta Materialia Phase field simulation of powder bed-
953 based additive manufacturing, Acta Mater. 144 (2018) 801–809.
954 https://doi.org/10.1016/j.actamat.2017.11.033.
955 [89] J.A. Dantzig, M. Rappaz, Solidification, EPFL Press, 2009.
956 [90] A.A. Martin, N.P. Calta, S.A. Khairallah, J. Wang, P.J. Depond, A.Y. Fong, V.
957 Thampy, G.M. Guss, A.M. Kiss, K.H. Stone, C.J. Tassone, J. Nelson Weker, M.F.
958 Toney, T. van Buuren, M.J. Matthews, Dynamics of pore formation during laser
959 powder bed fusion additive manufacturing, Nat. Commun. 10 (2019) 1–10.
960 https://doi.org/10.1038/s41467-019-10009-2.
961 [91] G. Vastola, Q.X. Pei, Y.W. Zhang, Predictive model for porosity in powder-bed fusion
962 additive manufacturing at high beam energy regime, Addit. Manuf. 22 (2018) 817–
963 822. https://doi.org/10.1016/j.addma.2018.05.042.
964

Supplementary Information

Porosity Percentage Calculation

The percentage of porosity in the samples was calculated using the μCT data. The total volume of the track above the substrate, with all pores filled, was measured. It is not possible to determine the volume of remelting into the substrate from the μCT scan, however a basic estimation has been calculated using a boundary box at the widest parts of the track, and a depth into the substrate at the deepest keyhole for each condition. This volume plus the track volume (above the substrate) were used as the estimation for total track volume. The volume porosity was then calculated as a percentage of this. This is a slight overestimation of total track volume, and thus underestimation of porosity percentage. The error was calculated by estimating a triangular section through the substrate, using the width of the boundary box and depth of the keyhole pores. This gave an error of 2 – 6 % for the porosity percentage calculation.

Supplementary Table 1

Linear energy density values from previous work and the present study. Hatch spacing has not been included in this calculation ($LED = P/vt$) for direct comparison to the energy densities presented here.

Laser Power, P (W)	**Scan Speed, *v* (mm s^{-1})**	**Powder layer thickness, *t* (mm)**	***LED* (J mm^{-2})**	**Reference**
175 – 400	500 – 1100	0.03	12	[1]
275	750	0.05	7.3	[2]
400	50 – 125	0.25	13 - 32	[3]
100	560	0.04	4.5	[4]
100 – 400	400 – 1600	0.05	5 - 10	[5]
42	200	0.03	7	[6]
200	200 – 400	0.1	5 – 10 (nominal) 3 – 9 (adjusted)	**Present work**

Supplementary Figure 1: Graphs showing the change in layer 5 deposited powder thickness in (**a**) Sample A, (**b**) Sample C, and (**c**) Sample D.

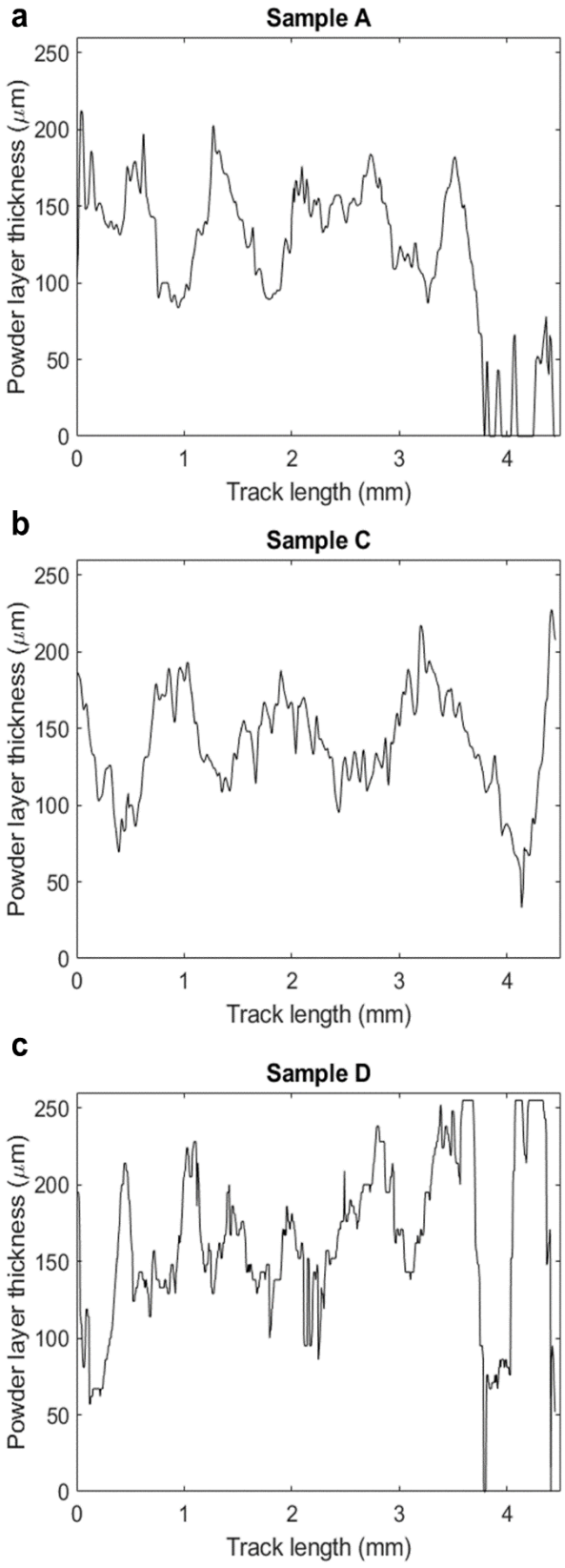

Supplementary Figure 2: (**a**) Background corrected but unedited radiograph of Sample A layer 3 final morphology, with red highlighted region correlating to (b – d) in **Figure 3**. (**b**) Background, GC plate surface, and excess powder removed from the image to highlight surface shape. A section on this image was taken for **Figure 3c**.

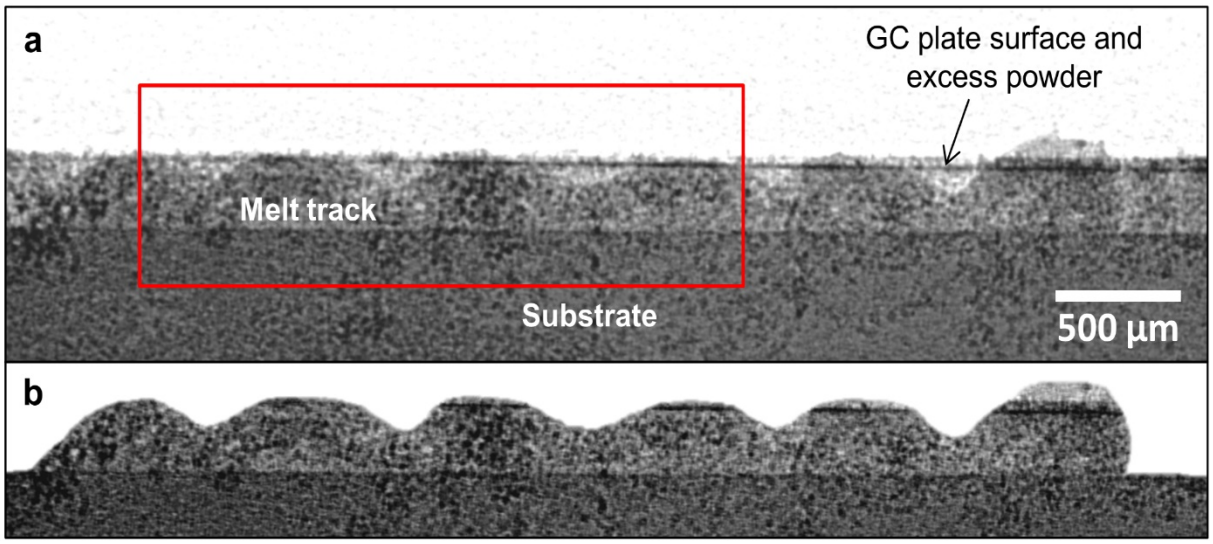

Supplementary Figure 3: SEM image of Sample D, showing partially melted powder particles adhered to the track surface.

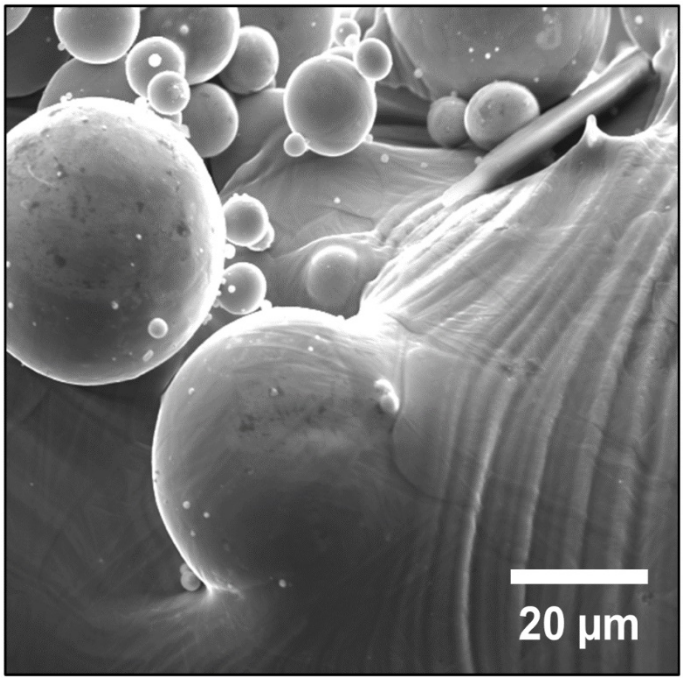

Supplementary Video 1: Sample A, Layer 1, showing *ca.* 50 μm build height, and laser keyhole *ca.* 150 μm below the powder surface.

Supplementary Video 2: Sample A, Layer 5, showing uneven track surface, and a large amount of powder and particle spatter.

Supplementary Video 3: Sample C, Layer 5, showing prominent surface undulations.

Supplementary Video 4: Sample D, Layer 5, showing uneven track surface and lack of fusion porosity between layers.

Supplementary Video 5: Sample B, Layer 5, showing large surface undulations and spatter, with a deep keyhole up to *ca.*250 μm below the powder surface.

Supplementary Video 6: Sample B, Layer 5, background subtracted image to highlight powder layer thickness (dark grey), keyhole, and track undulations.

Supplementary Video 7: Sample C, Layer 1, showing *ca.* 100 μm track height at the ends of the track, with *ca.* 30 μm track height in the centre of the track. Powder spatter and porosity formation is visible. The keyhole depth was *ca*. 215

μm below the powder surface.

Supplementary Video 8: Sample C, Layer 1, cropped to ROI for keyhole porosity formation in the substrate.

Supplementary Video 9: Sample C, Layer 1, cropped to ROI, and locally averaged to reveal changing keyhole shape and size. Averaging method removes visible pores once they become stationary within the track.

Supplementary Video 10: Sample C Layer 2, full track, showing slight variations in track height and deep laser penetration, remelting all of layer 1.

Supplementary Video 11: Sample C, Layer 2, cropped to ROI for keyhole porosity formation in the substrate.

References

[1] O. Andreau, I. Koutiri, P. Peyre, J.D. Penot, N. Saintier, E. Pessard, T. De Terris, C. Dupuy, T. Baudin, Texture control of 316L parts by modulation of the melt pool morphology in selective laser melting, J. Mater. Process. Technol. 264 (2019) 21–31. https://doi.org/10.1016/j.jmatprotec.2018.08.049.

[2] B. Shen, H. Li, S. Liu, J. Zou, S. Shen, Y. Wang, T. Zhang, D. Zhang, Y. Chen, H. Qi, Influence of laser post-processing on pore evolution of Ti–6Al–4V alloy by laser powder bed fusion, J. Alloys Compd. 818 (2020) 152845. https://doi.org/10.1016/j.jallcom.2019.152845.

[3] W. Shi, P. Wang, Y. Liu, Y. Hou, G. Han, Properties of 316L formed by a 400 W power laser Selective Laser Melting with 250 μm layer thickness, Powder Technol. 360 (2020) 151–164. https://doi.org/10.1016/j.powtec.2019.09.059.

[4] M. Hirsch, P. Dryburgh, S. Catchpole-Smith, R. Patel, L. Parry, S.D. Sharples, I.A. Ashcroft, A.T. Clare, Targeted rework strategies for powder bed additive manufacture, Addit. Manuf. 19 (2018) 127–133. https://doi.org/10.1016/j.addma.2017.11.011.

[5] C. Tang, K.Q. Le, C.H. Wong, Physics of humping formation in laser powder bed fusion, Int. J. Heat Mass Transf. 149 (2020) 119172. https://doi.org/10.1016/j.ijheatmasstransfer.2019.119172.

[6] L. Thijs, F. Verhaeghe, T. Craeghs, J. Van Humbeeck, J.P. Kruth, A study of the microstructural evolution during selective laser melting of Ti-6Al-4V, Acta Mater. 58 (2010) 3303–3312. https://doi.org/10.1016/j.actamat.2010.02.004.